Towards simulating convection in substellar objects.

Dissertation

zur Erlangung des Doktorgrades

des Department Physik

der Universität Hamburg

vorgelegt von

Veronica Arias Callejas

aus Bogotá, Colombia

Hamburg

2012

Gutachter der Dissertation:
Prof. Dr. Peter H. Hauschildt
Prof. Dr. Stefan Dreizler

Gutachter der Disputation:
Prof. Dr. Robi Banerjee
Prof. Dr. Jürgen H.M.M. Schmidt

Datum der Disputation: 16 Juli 2012

Vorsitzender des Prüfungsausschusses: Dr. Robert Baade

Vorsitzender des Promotionsausschusses: Prof. Dr. Peter H. Hauschildt

Leiter des Departaments Physik: Prof. Dr. Daniela Pfannkuche

Dekan der MIN-Fakultät: Prof. Dr. Heinrich Graener

Abstract

The study of substellar objects is a rapidly growing field. Since the 1995 discovery of the first brown dwarf and the first extrasolar giant planet—around a main sequence star—, hundreds of these substellar objects have been detected, providing fascinating information to test evolutionary and formation models. The recent great advances in the quality of the observations provide valuable insights, and inspire the development of more realistic and detailed models of the physical processes that govern these objects. Substellar objects are mostly fully convective and have molecular atmospheres with complex chemical processes. As the dominant energy transport mechanism, convection determines the temperature structure of these objects. Additionally, temperature and density anomalies associated with convection generate up-flows and down-flows of material that are responsible for transporting the various chemical species between different layers. These complex and inherently 3D convective dynamics cannot be completely described by the widely used 1D mixing length theory (MLT) approximation, requiring the use of arbitrary parametrizations. 3D radiative-hydrodynamic simulations of solar convection have become a valuable tool to study the convective dynamics, and its results are in very good agreement with solar observations. In recent years, cooler objects have been studied using 3D simulations, with a special focus on the effect of convection on the M-dwarf spectral lines. This work is a first step in the development of a reliable numerical tool that is capable of simulating convection in 3D for substellar objects, and focuses on the convective dynamics in combination with the equation of state.

For that purpose, we coupled and tested a sophisticated equation of state (ACES-EOS) to the hydrodynamic FLASH code that includes chemical processes such as molecule formation and handles temperatures as low as 100K. However, before we could use the "FLASH+ACES-EOS" code in the substellar regime, we needed to test it against other existing 3D simulations and chose an M-dwarf—cold and dense enough for molecules to play a significant role—for which 3D models exist. In this M-dwarf test simulation using the "FLASH+ACES-EOS" code, we found granule-like structures with warmer and less dense regions moving upwards and colder denser regions moving downwards. The "FLASH+ACES-EOS" temperature, density and pressure altitude-mean-profiles are in very good agreement with PHOENIX/1D models and the rms z-velocity values of around 0.2km/s are similar to those obtained by previous studies. All these results indicate that convection is correctly simulated by the FLASH code coupled to the ACES-EOS. With this validation process completed, it is possible in future work to perform simulations of objects with lower temperatures and lower masses.

Abstract

Das Studium substellarer Objekte ist ein schnell wachsendes Feld. Seit 1995 und der Entdeckung des ersten braunen Zwerges und des ersten extrasolaren Gasriesen -um einen Hauptreihenstern- wurden hunderte substellare Objekte nachgewiesen, die faszinierende Informationen zum Testen von Evolutions- und Bildungsmodellen liefern. Die gegenwärtig schnell voranschreitende Qualität von Beobachtungen erbringen wertvolle Erkenntnisse und inspirieren zur Entwicklung zunehmend realistischer und detaillierter Modelle all der bedeutenden physikalischen Prozesse dieser Objekte. Substellare Objekte sind häufig vollkonvektiv und verfügen über molekulare Atmosphären mit komplexen chemischen Prozessen. Als dominanter Energietransportmechanismus, bestimmt Konvektion über die Temperaturstruktur dieser Objekte. Zusätzlich bewirken konvektionsbedingte Temperatur- und Dichteanomalien auf- und abwärtsgerichtete Materialströmungen, welche verantwortlich für den Transport chemischer Spezies zwischen den verschiedenen Atmosphärenschichten sind. Die komplizierte Dynamik der natürlichen dreidimensionalen Konvektion kann nicht vollständig durch die weitverbreitete Approximation der 1D Mischungswegtheorie beschrieben ohne zusätzliche, willkürliche Parametrisierung. Existierende lokale 3D Strahlungs-/Hydrodynamiksimulationen von solarer Konvektion sind zu einem wertvollem Hilfsmittel zum Studium konvektiver Dynamik geworden, wobei deren Ergebnisse gut mit Sonnenbeobachtungen übereinstimmen. In den letzten Jahren wurden zunehmend kühlere Objekte mittels 3D-Simulationen studiert, mit besonderer Ausrichtung auf deren Auswirkung auf M-Zwerg Spektrallinien. Diese Arbeit stellt einen ersten Schritt in der Entwicklung eines zuverlässigen, numerischen Werkzeugs dar, das in der Lage sein wird, dreidimensionale Konvektion in substellaren Objekte zu simulieren, und konzentriert sich konvektiver Dynamik in Verbindung mit der Zustandsgleichung.

Aus diesem Grund, haben wir eine moderne Zustandsgleichung (ACES-EOS) in den Hydrodynamik-Code FLASH integriert und getestet, welche chemische Prozesse wie Molekülbildung beinhaltet und für Temperaturen bis herunter zu 100K anwendbar ist. Dennoch, bevor der "FLASH+ACES-EOS" Code für das substellare Regime angewendet werden kann, mussten wir ihn zuerst an existierenden 3D Simulationen testen und entschieden uns für einen M-Zwerg - kühl und dicht genug, sodass Moleküle eine wichtige Rolle spielen - da entsprechende 3D Modelle existieren.

In den M-Zwerg Testsimulationen mit dem "FLASH+ACES-EOS" Code fanden wir granulenartige Strukturen bestehend aus warmen, weniger dichten Regionen in Aufwärtsbewegung und kälteren, dichteren Regionen in Abwärtsbewegung. The schichtweise gemittelten Temperatur-, Dichte- und Druckprofile der "FLASH+ACES-EOS" Simulationen sind in guter Übereinstimmung mit PHOENIX/1D Modellen und das quadratische Mittel der z-Geschwindigkeitskomponenten von etwa 0,2km/s sind vergleichbar mit Ergebnissen früherer Studien. All diese Ergebnisse zeigen, dass Konvektion korrekt durch den FLASH Code mit integrierter ACES-EOS simuliert werden. Mit dem Abschluss dieses Validisierungsprozesses ist es in zukünftigen Arbeiten möglich, Simulationen für Objekte niedrigerer Temperaturen und Massen durchzuführen.

Contents

1 Introduction **7**

1.1 Substellar objects 7
1.2 Convection 8
1.3 Euler equations and the equation of state 9
1.4 Aim and outline of the thesis 10

2 Adapting the FLASH code **13**

2.1 The FLASH grid 13
2.2 The Hydro-dynamical solver 14
2.3 ACES equation of state 19
2.3.1 Internal energy and entropy calculation 20
2.3.2 Γ and γ calculation 21
2.3.3 ACES-EOS and Γ Tests 22

3 Simulation setup **27**

3.1 The simulation domain: A box in the star or a star in a box? 27
3.2 Boundary conditions 29
3.3 PHOENIX/1D atmosphere models 31

4 Results **33**

4.1 Characterizing convection 33
4.1.1 Evidence of convection: looking for a granulation pattern. 34
4.1.2 Up-flows, down-flows and their correlation with temperature and density. 35
4.1.3 Vertical profiles and comparison to PHOENIX/1D models 37
4.1.4 Vertical velocity analysis 42
4.2 Impact of the inital and boundary conditions 43
4.2.1 Initial conditions and different box sizes 44
4.2.2 Lower boundary internal energy 48
4.3 Tuning the lower boundary internal energy. 49
4.4 Impact of the upper boundary internal energy. 56
4.5 Discussion: stability of the simulations 58
4.6 A higher resolution simulation 61

5 Conclusions and outlook 67

Bibliography 71

Acknowledgement 75

Chapter 1

Introduction

1.1 Substellar objects

The term "substellar object" encompasses two conceptually different but physically closely related classes of objects: brown dwarfs and extrasolar giant planets. Brown dwarfs form like stars, but have masses smaller than around 0.075 solar masses ($M_{\odot}$), and never reach large enough densities and pressures to mantain continuous thermonuclear reactions in their cores. Despite a temporary deuterium and lithium burning phase, the lack of sustained thermonuclear reactions— brown dwarfs have no stable hydrogen burning phase—results in no mechanism to compensate for the surface radiative losses, making these objects cool down continuosly(e.g., Burrows et al., 2001). On the other hand, extrasolar giant planets form in a protoplanetary disk. It is the difference in their formation mechanism that differenciates a brown dwarf from a giant planet. A clasification based on the mass, that defines a planet as an object having a mass smaller than 13 Jupiter masses ($M_{\rm jup}$) can be misleading since, as discussed by Baraffe et al. (2010), there is an overlap in mass between the brown dwarfs and the extrasolar giant planets, with evidence of a planet more massive than 13 $M_{\rm jup}$ and brown dwarfs with masses smaller than 13 $M_{\rm jup}$. In addition to observational evidences, stellar formation simulations also succesfully form "planetary mass" brown dwarfs (Whitworth and Stamatellos, 2006).

Due to their low masses and lack of thermonuclear burning in their cores, old (high surface gravity) substellar objects have effective temperatures of roughly 2000K and lower. These objects are mostly fully convective and have molecular atmospheres with complex chemical processes and dust formation (Chabrier et al., 2004). Convection is the dominant energy transport mechanism, except at the thin radiative outermost layer. It determines the temperature structure of the object and is also responsible for the chemical mixing. In the majority of the evolutionary and atmospheric models, the mixing length theory (MLT) approximation (e.g., Hansen and Kawaler, 1994) is used to account for convection. This approximation has two main limitations. First, it uses an arbitrary parameter (a mean free path of a convective element), which can only be tuned for the solar convection. And second, the MLT is a 1D approx-

imation, so it cannot describe the complex 3D dynamics that occur in a convective system and influence the surrounding non-convective layers. This 3D dynamics can have significant effects on the resulting spectra, since on the one hand, they efficiently mix the different chemical species present—transporting them from deeper to shallower layers—and on the other hand, the convective velocity fields as well as the temperature anomalies can distort the line profiles. Therefore, in order to construct more realistic atmospheric models, a 3D treatment of convection is required.

There are several detailed 3D radiative-hydrodynamic simulations of solar convection (e.g., Stein and Nordlund, 1998), for which the results are in very good agreement with observations. For objects cooler that the sun, there are a series of 3D simulations by Ludwig (2006) and Wende et al. (2009) for M-dwarfs, and 2D simulations by Freytag et al. (2010) for M and brown dwarfs. The current work is an effort in the direction of having reliable 3D hydrodynamic simulations of convection for substellar objects. But before we discuss in more detail our approach to the problem, it is convenient to describe how convection instabilities arise and to briefly explain the hydrodynamic equations that need to be considered in convective simulations as well as the role played by the equation of state.

1.2 Convection

When we study the interiors and atmospheres of stars or substellar objects, we are dealing with a stratified gas that has a given density, temperature and pressure gradient. Energy is transported from the hotter core of the object to the surface, where radiative losses occur. There are two main energy transport mechanisms: convection and radiation, and depending on the density, pressure and temperature gradients and on the resulting properties of the gas (such as opacity), one of the two energy transport mechanisms is dominant.

In the case of convection, the energy is transported by gas displacements. This occurs when the stratification is unstable against convection. That is, when the environment surrounding a rising parcel of gas is such that this parcel is further accelerated upwards as it rises. Conceptually, the stability of the fluid against convection can be understood by analyzing what happens if a parcel of fluid rises a distance Δz: will it continue to rise, or will it sink towards its original position? If the parcel continues to rise, the stratified gas is convectively unstable, but if it returns to the initial position, the stratified gas is stable against convection. The answer to this question depends on the thermodynamical process that the parcel undergoes as it moves. The parcel rises approximately addiabatically—without exchanging heat with its surroundings—and expands reaching pressure equilibrium with the surrounding fluid almost immediately. In this expansion process, the parcel's density and temperature decrease. If the new density is lower that that of the surrounding gas, the parcel is bouyant, and will continue

to rise: in this case, the system is unstable against convection. On the other hand, if the new density is higher than that of the surrounding fluid, the parcel will tend to sink, generating the so-called buoyancy oscillations.

This stability condition can be expressed in terms of density gradients, where the density change experienced by the rising parcel is associated, to a first order approximation, to the adiabatic gradient $(d\rho/dz)_{ad}$ and to the environment's density gradient $(d\rho/dz)_{env}$. The system is unstable against convection if $(d\rho/dz)_{ad}<(d\rho/dz)_{env}$. This criterion is is known as the "Schwarzschild criterion". For a more detailed description, see Mihalas and Mihalas (1984).

1.3 Euler equations and the equation of state

The dynamics of a compressible inviscid fluid are governed by a set of conservation equations: the conservation of mass, momentum and energy. These equations are derived in numerous textbooks (e.g., Mihalas and Mihalas, 1984), and, therefore, are described only briefly here.

The first equation, known as the equation of continuity, results from the principle of mass conservation. The mass of any arbitrary volume can only change if there is a net mass flux through the enclosing surface. Therefore, any change in density must be necessarily related to mass flux convergence/divergence:

$$\frac{\partial \rho}{\partial t} + \nabla \cdot (\rho \vec{u}) = 0, \tag{1.1}$$

where $\vec{u}$ is the fluid velocity.

The second equation, the conservation of momentum, results from Newton's second law applied to an arbitrary volume of inviscid fluid. It is similar to the continuity equation above, except that we must also consider forces acting on the volume, which modify the total momentum. We can distinguish two types of forces: "body forces", like gravity $\vec{g}$, which act on all the fluid elements contained in the volume, and "surface forces", like pressure P, that act on the surface enclosing the volume. The resulting momentum equation is actually a system of 3 equations, one for each spatial dimension:

$$\frac{\partial (\rho \vec{u})}{\partial t} + \nabla \cdot (\rho \vec{u} \vec{u}) + \nabla P = \rho \vec{g} \tag{1.2}$$

Note that this is a particular case of the more general Navier-Stokes equations, which would additionally include viscous forces.

For the energy conservation equation, we consider only the specific internal energy E_{int} (see Section 2.3.1 for details on how we calculate it) and the specific kinetic energy $E_{\text{kin}} = u^2/2$. The total energy associated to an arbitrary volume of fluid is the volume integral of $\rho E_{\text{tot}} = \rho(E_{\text{int}} + E_{\text{kin}})$. Changes in the total energy are a result of energy advection through the surface of the control volume, or due to work done by the exterior on the control volume (as stated in the first law of thermodynamics). The resulting energy conservation equation is:

$$\frac{\partial(\rho E_{\text{tot}})}{\partial t} + \nabla \cdot [(\rho E_{\text{tot}} + P)\vec{u}] = \rho \vec{u} \cdot \vec{g} \tag{1.3}$$

Equations (1.1) through (1.3) are known as the Euler equations and can be used to calculate the dynamics of inviscid and compressible fluids. Nevertheless, these five equations relate six independent variables: density ρ , pressure P, temperature T and the three components of the velocity vector $\vec{u}$. Therefore, an additional closure condition is required in order to solve the system of equations.

This closure condition is the equation of state (EOS) that relates the various thermodynamic variables of the fluid. Note that the complexity of this EOS will depend on the properties of the fluid of interest. The most simple example is the ideal gas EOS, which assumes no interaction between the components of the gas other than elastic collisions. However, for the temperature and density ranges encountered in very low-mass stars and substellar objects, chemical processes—such as molecule formation—occur and play a significant role in the thermodynamics of the system. Since the ideal gas EOS ignores all chemical processes, it is not suitable for studying substellar objects. Therefore, we require a more complex and realistic EOS. We use the "Astrophysical Chemical Equilibrium Solver" (ACES) EOS, which is a module of the PHOENIX code (Hauschildt and Baron, 2011), and has been widely tested and successfully used for numerous simulations of atmospheres of sub-stellar objects (e.g., Witte et al., 2011). A more detailed description of this ACES-EOS can be found in Section 2.3.

1.4 Aim and outline of the thesis

The aim of the current thesis is to advance towards constructing reliable 3D hydrodynamic simulations of convection in substellar objects. For that purpose, one of the main steps of this work is to couple an adequate and detailed EOS to a general hydrodynamic code that solves the above described Euler equations. We use the FLASH hydrodynamic solver and couple to it the "Astrophysical Chemical Equilibrium Solver" (ACES) EOS. This EOS can handle temperatures as low as 100K, which covers almost the whole temperature range of substellar objects. However, it is necessary to first set up an appropriate model and validate the "FLASH

+ ACES-EOS" for a "known" case. This is what this study aims at. We do this for a test M-dwarf, for which we can use results from simulations by Wende et al. (2009) and Freytag et al. (2010) for comparison purposes. Once this is successfully tested, future studies can proceed to use the same "FLASH+ACES-EOS" code to model colder substellar objects.

The structure of this thesis is as follows: the current Chapter presents an introduction to the hydrodynamic simulation of substellar objects and describes the main aim of this study. In Chapter 2, we describe the modifications performed to the hydrodynamic solver in the FLASH code (Fryxell et al., 2000), and in particular the coupling and testing of the equation of state (ACES-EOS) (Hauschildt and Baron, 2011). With the new ACES-EOS coupled to the FLASH code, we proceed in Chapter 3 to setup appropiate boundary and initial conditions for a test simulation of an M-dwarf. In Chapter 4, the results of the hydrodynamic simulation are presented, analyzed and compared to other models, followed by several tests on the sensitivity of the results to changes in the initial and boundary conditions, as well as on the domain size and resolution. Finally, Chapter 5 summarizes the main conclusions that we obtained together with an outlook for future studies.

Chapter 2

Adapting the FLASH code

We use the FLASH code to simulate convection in the upper part of the convective layers of sub-stellar objects. This code was partly developed by the DOE-supported ASC/Alliance Center for Astrophysical Thermonuclear flashes at the University of Chicago (Fryxell et al., 2000). There are several reasons why we have selected the FLASH code. One is the code's architecture: the FLASH code is modular, which allows users to configure initial and boundary conditions, add new physical effects, and include their own equation of state. Another reason is that the FLASH code is parallelized: it uses the Message Passing Interface (MPI) which ensures portability and good performance. And finally this code has been successfully tested for a wide range of astrophysical problems, for example modeling supernovae (Couch et al., 2011), star formation (Banerjee and Pudritz, 2007) and protoplanetary disks (de Val-Borro et al., 2007), among many others. In the following sections briefly describe the most relevant features of the code and of the modifications necessary for the simulation of convection in sub-stellar objects.

2.1 The FLASH grid

The FLASH code uses the PARAMESH package (MacNeice et al., 2000), which is based on a block-structured Adaptive Mesh Refinement (AMR) method. AMR can be very useful for simulations that cover various spatial scales and where some small regions of the simulation domain need to be studied with high resolution. But convection is an ubiquitous phenomenon so AMR does not present any benefits for our particular simulations. Therefore, we will not describe here any of the AMR refinement and de-refinement processes and we will limit ourselves to a brief description of the PARAMESH block structure and the code parallelization.

The simulation domain in the FLASH code is divided into blocks that are further divided into interior grid cells (see Figure 2.1). Each cell is a physical volume element and has a set of hydrodynamical and thermodynamical data asociated to it. For computational purposes, each block is surrounded by guard cells. These guard cells either overlap with the interior cells of neighboring blocks—and are therefore filled with the data from those neighboring interior

cells—or are at the domain boundary—and are therefore filled according to the boundary conditions. A more detailed description of how the boundary guard cells are filled can be found in section 3.2. The "block + guard cell" decomposition of the domain allows for the hydrodynamic calculations to be done independently for each block. PARAMESH handles the block distribution among available processors as well as the inter-processor and inter-block communications.

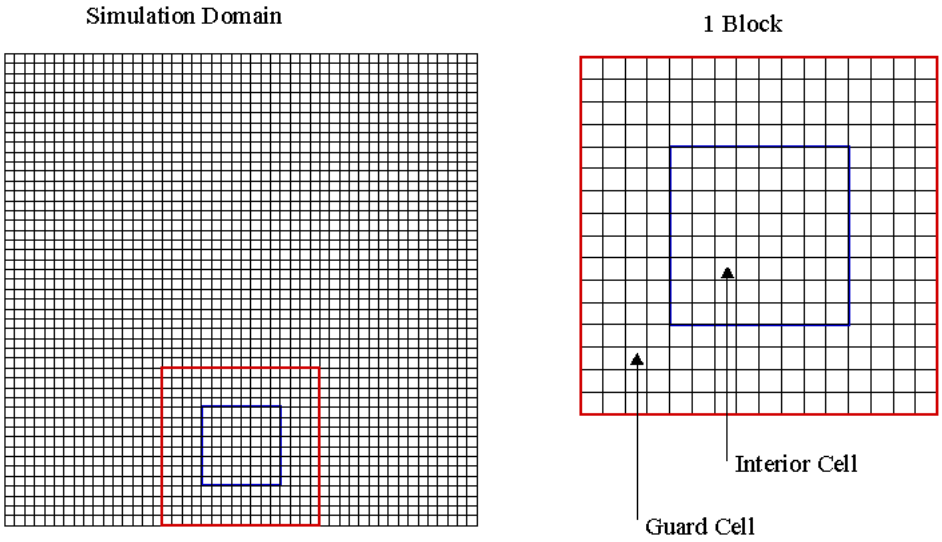

Figure 2.1: The simulation domain in the left panel is divided into blocks (framed by the blue lines). The right panel shows how each block is divided into cells (also called interior cells) and is surrounded by guard cells (framed by the red lines)

2.2 The Hydro-dynamical solver

The FLASH code solves the 3D Euler equations (see Section 1.3) using a directionally split piecewise-parabolic method (PPM) solver (Colella and Woodward, 1984). The PPM method implemented in FLASH is the direct Eulerian method and is a higher order version of the Godunov method (Godunov, 1959). The Euler equations are a set of equations that determine the evolution of the following conserved quantities: mass, momentum (x, y, z) and total energy. The FLASH code is a grid based hydrodynamical code that stores, in each of its grid cells, a cell averaged value of each of the conserved quantities. Therefore, the PPM method is a finite-volume method since it deals with averaged values of the conserved quantities that are associated with a grid cell and not with a specific point in space. In general, this method

consists of three main steps: First, a "reconstruction step", in which a piecewise function is constructed from the averaged values of the conserved quantities in each of the cells at time t_n. Then, during the "solution step", a numerical solution of the Riemann shock tube problem is calculated at the cell interfaces to obtain the time-advanced fluxes at the cell boundaries. Finally, these fluxes are used to solve a set of conservative differential equations to calculate and update the zone averaged values of the conserved quantities to the next time step t_{n+1}.

The "reconstruction step" in the PPM method can be a quite complex process. The Godunov method uses a piecewise constant function in the reconstruction step, whereas the PPM method uses a piecewise polynomial function to make the solution third order accurate. This piecewise function is constructed using a fourth order polynomial and has to satisfy monotonicity constrains. A more detailed description of the construction of the piecewise parabolic function is beyond the scope of this work and is given by Fryxell et al. (2000) and Colella and Woodward (1984).

The "solution step" updates the zone-averaged values of the conserved quantities to the next time step, solving conservative differential equations for each of the conserved quantities. To solve these equations, it is necessary to know the fluxes of the conserved variables through the zone interfaces. Unfortunately, it is not possible to obtain these fluxes directly from the piecewise parabolic function. That is because, in general, there are two different values (one for each cell), and because these flux values are asociated with t_n (instead of t_{n+1}) which would make the solution numerically unstable. To overcome that problem, FLASH uses a Riemann solver to calculate the time-advanced fluxes at each cell's interface.

The Riemann shock problem describes the evolution of two constant states that are separated by a discontinuity. For the solution step, effective left and right states have to be constructed at each cell's interface. These effective left and right states could be obtained by using an average value of the piecewise parabolic function, but this would yield the same result as the constant piecewise function, loosing all the effort invested in the construction of the piecewise polynomial function. Instead, the PPM solver constructs these effective left and right hand states in a more sophisticated way. Since all signals travel with a finite speed, not all the material within two consecutive cells can influence its interface during a time step. To determine the domain of dependence of the interface, backward characteristics with respect to time are traced from the cell's interface at t_{n+1}. Only the material within the characteristic and the interface can have an influence during the time step. Figure 2.2 shows the characteristics for the Lagrangian formulation (left panel) and compares it to the more complicated case of the Eulerian formulation characteristics of a subsonic flow (middle panel) and supersonic flow (right panel) with the fluid moving right. PPM does a correction of the left and right states to account for the number of characteristics on each side of the interface. Further details are given by Colella and Woodward (1984).

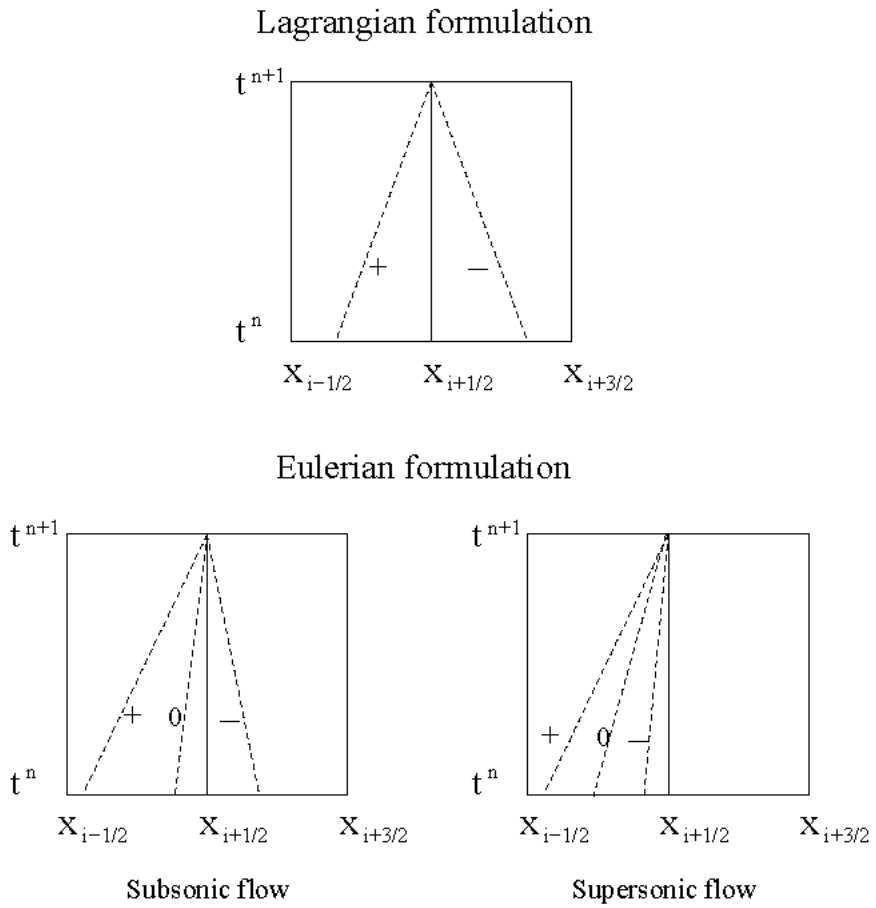

Figure 2.2: Shows schematically the different possibilities for the characteristics in the Riemann shock tube problem. The upper panel corresponds to the simpler case of the Lagrangian formulation, where the characteristics are symmetric at each side of the interface. The lower panel shows the characteristics for the Eulerian formulation. This case is more complicated since the fluid is moving (in this case to the right) with respect to the grid. The lower left panel corresponds to a subsonic flow, and the lower right panel to a supersonic flow.

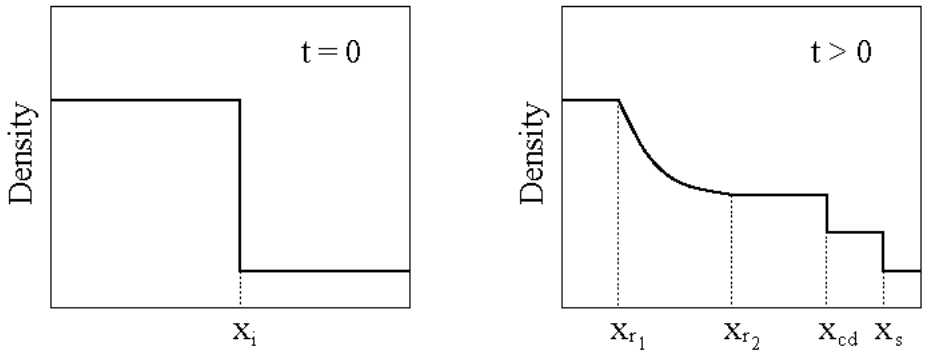

Figure 2.3: Schematic density profile at different times for the Riemann shock tube problem. On the left panel at t=0 the profile depicts the two initial states (corresponding to the left and right states at a grid cell's interface X_i) each with a constant density. In the right panel, for $t > 0$, the density profile exhibits the undisturbed left and right initial states, a rarefaction wave (from X_{r_1} to X_{r_2}), a contact discontinuity (at X_{cd}) and a shock wave (at X_s).

Once the left and right hand states have been properly constructed, FLASH proceeds to solve the Riemann's problem at each cell's interface. In Figure 2.3 we can see a scheme of the general solution of the Riemann shock tube problem, with a wave (in this case a rarefaction) traveling to the left, another wave (in this case a shock) traveling to the right, and between the two waves, a contact discontinuity. For performance reasons, the solver in the FLASH code treats both left and right waves as shocks. As described by Fryxell et al. (2000), the equation for a shock moving to the left is

$$P^* - P_l + W_l(u^* - u_l) = 0, \tag{2.1}$$

and for a shock moving to the right

$$P^* - P_r + W_r(u^* - u_r) = 0, \tag{2.2}$$

where P is the pressure, u is the flow velocity and W is the wave speed. The superscript * refers to the post-shock state and the subscripts $_l$ and $_r$ stand for the pre-shock left and right states. For the specific case of the ideal gas equation of state, the wave velocity W_s is given by

$$W_s = C_s \left[1 + \frac{\gamma + 1}{2\gamma} \left(\frac{P^* - P_s}{P_s} \right) \right]^{\frac{1}{2}} \tag{2.3}$$

where γ is the adibatic index, the subscripts $_s$ denotes the shock state and C_s is the Lagrangian sound speed velocity

$$C_s = (\gamma_s P_s \rho_s)^{\frac{1}{2}}. \tag{2.4}$$

A non-ideal gas equation of state has four adiabatic indexes as described by Chandrasekhar (1957). The FLASH code uses a parameterization method developed by Colella and Glaz (1985) that reduces the four adiabatic indexes to two. These two adiabatic indexes are variables that depend on the thermodynamical data and can be calculated using the relations

$$\Gamma = \left(\frac{\partial \ln P}{\partial \ln \rho} \right)_S \tag{2.5}$$

and

$$\gamma = 1 + \frac{P}{\rho \epsilon}, \tag{2.6}$$

where ρ denotes density and ϵ internal energy. This adds two extra complications to the Riemann solver. First there are now two adiabatic indexes instead of one, and second, these adiabatic indexes can have different values for each of the cells. With these new considerations the approximate nonlinear wave speed is (Fryxell et al., 2000),

$$W_s^2 = \rho_s (P^* - P_s)(\gamma_s - 1) \frac{P^* + 0.5(\gamma_s^* - 1)(P^* + P_s)}{(\gamma_s - 1)P^* - (\gamma_s^* - 1)P_s} \tag{2.7}$$

with

$$\gamma_s^* = \gamma_s + 2(\hat{\gamma} - 1) \left(\frac{\hat{\gamma}}{\hat{\Gamma}} \right) \frac{P^* - P_s}{P^* + P_s} \tag{2.8}$$

where

$$\hat{\Gamma} = \frac{1}{2}(\Gamma_l + \Gamma_r) \tag{2.9}$$

and

$$\hat{\gamma} = \frac{1}{2}(\gamma_l + \gamma_r). \tag{2.10}$$

Using equations (2.1) and (2.2), and the appropriate adiabatic indexes, it is possible to calculate the fluxes through the interface. Further details of how this is carried out are described by Toro (2009) for general cases, or by Colella and Woodward (1984) and by Colella and Glaz (1985) for the specific PPM method. Once the fluxes are obtained, a set of conservative differential equations are solved to calculate and update the cell averaged values of the conserved quantities to the next time step.

All the above descriptions of the Hydro-dynamical solver correspond to a 1D problem. For a 3D case a method called dimensional splitting or Strang splitting is used (Strang, 1968). This method solves the 3D equations as a succession of 1D problems. A directional sweeping is done in the order xyz-zyx, and a small multidimensional artificial viscosity is included to provide a weak coupling between adjacent rows and columns (Fryxell et al., 2000).

2.3 ACES equation of state

An equation of state (EOS) is a relation between the various thermodynamic variables of a fluid. In the FLASH code, after the hydrodynamical solver calculates the density and energy at $t = t_{n+1}$, the EOS is used to obtain the temperature, pressure and other thermodynamic variables at $t = t_{n+1}$. As was described in the previous section, in the general case of a non-ideal gas EOS, the adiabatic index Γ plays a crucial role in the Riemann solver, so that properties of the EOS not only determine the temperature and pressure values for a given energy and density, but also determine the dynamics of the fluid.

The FLASH code provides two different EOS modules: an ideal gas EOS module and a Helmholtz EOS module. Since we simulate convection in sub-stellar objects, we need an EOS that handles in detail the chemical processes associated with low temperatures (in particular molecule formation), i.e., that has a detailed treatment of the chemical composition. The ideal gas EOS ignores the chemical processes in the gas and the Helmholtz EOS does not handle temperatures below 10000 K, so it would be inadequate from a physical point of view to use any of the EOS provided by FLASH for our specific problem. Hence, a crucial aspect of this work is the coupling of an appropriate EOS to the FLASH code.

We use the "Astrophysical Chemical Equilibrium Solver" (ACES) EOS which is a module of the PHOENIX code (Hauschildt and Baron, 2011). This ACES-EOS has been widely tested and successfully used for a wide range of simulations of atmospheres of sub-stellar objects (e.g. Witte et al., 2011). The ACES-EOS works schematically as follows: given an elemental composition (we are using solar composition) and a temperature and pressure, the EOS sweeps over the possible configurations of molecules, ions and atoms that can result, and looks for the configuration that minimizes the energy. Then, for that configuration, the ACES-EOS calculates the corresponding density and internal energy. Details on both the theoretical and numerical methods behind this EOS are described in detail by Smith and Missen (1982).

The above described procedure is repeated for various values of temperature and pressure to generate a temperature-pressure ACES-EOS table. This table is then re-mapped into a density-energy EOS table, since the hydrodynamical solver provides the EOS with the density and internal energy values and expects the pressure and temperature values in return. We implemented a new EOS sub-unit in the FLASH code that reads and stores the ACES-EOS table in a way that the Hydro-dynamical solver can access all the required quantities.

The ACES-EOS is a module of the PHOENIX code that has been widely used in radiative transfer simulations (Witte et al., 2011). Nevertheless, there are thermodynamical quantities that the ACES-EOS provides specifically for our hydrodynamical simulations. These are the internal energy and the entropy. We also need to calculate the adiabatic indexes Γ and γ. In the following we briefly describe how these thermo-dynamical quantities are obtained and tested.

2.3.1 Internal energy and entropy calculation

The internal energy and the entropy can be calculated using the partition function Z of the gas. The following description is based on the Boltzmann statistics treatment of the gas and all the equations we reproduce here are derived in detail by Mihalas and Mihalas (1984).

A system consisting of N particles inside a volume V and with a total internal energy $E_{\rm int}$ can be described by a distribution function based on the assumption that the particles are distributed among cells with energy ϵ_i. The number of particles in the $i_{\rm th}$ cell is given by the occupation number ν_i, and a set of i occupation numbers $\{\nu_i\}$ has to satisfy that the total number of particles is $N = \sum_i \nu_i$ and the total internal energy is $E_{\rm int} = \sum_i \nu_i \epsilon_i$. In principle, there are many sets of occupation numbers that satisfy the conditions on N and $E_{\rm int}$. Nevertheless it can be shown that there is only one that maximizes the entropy of the system. The partition function associated with this set of $\{\nu_i\}$ is defined as

$$Z = \sum_i g_i \exp(-\epsilon_i / kT), \tag{2.11}$$

where T is the temperature of the system, k is the Boltzmann constant and g_i is a weight function associated with the degeneracy of the $i_{\rm th}$ cell. The total internal energy of the system can be obtained from the partition function as follows

$$E_{\rm int} = NkT^2 \left(\frac{\partial \ln Z}{\partial T} \right)_{\upsilon}. \tag{2.12}$$

The partition function Z can be expressed as the product of the translational energy component $Z_{\rm trans}$ and electron energy component$Z_{\rm ele}$ as follows: $Z = Z_{\rm trans} Z_{\rm ele}$. Equation (2.12) can be then rewritten as the sum of the translational energy term $E_{\rm trans}$ and the the electron energy term $E_{\rm ele}$:

$$E_{\rm int} = E_{\rm trans} + E_{\rm ele} = \frac{3}{2} NkT + NkT^2 \left(\frac{\partial \ln Z_{\rm ele}}{\partial T} \right)_{\upsilon}. \tag{2.13}$$

The translational term $E_{\rm trans}$ can be easily calculated from the temperature, whereas the electron energy term $E_{\rm ele}$ needs the $Z_{\rm ele}$ values to be calculated. In order to obtain $Z_{\rm ele}$, the ACES-EOS sweeps over all the molecules, atoms and ions that exist in the system to obtain the $(\partial \ln Z_{\rm ele}/\partial T)_{\upsilon}$ values that are required to calculate the internal energy of the system.

The entropy S of the system can be calculated as well from the partition function

$$S = Nk\left[\frac{5}{2} + \ln\left(\frac{V}{N}\right) + \ln\left(\frac{(2\pi mkT)^{3/2}}{h^3}\right)\right] + R\left[\ln Z_{\text{ele}} + T\left(\frac{\partial \ln Z_{\text{ele}}}{\partial T}\right)_{\upsilon}\right], \quad (2.14)$$

and it is possible, again, to relate the first term to the translational energy component of the partition function, and the second term to the electron energy component. Once again, both terms can be calculated from the temperature and the Z_{ele} values calculated by the ACES-EOS.

2.3.2 Γ and γ calculation

For a general equation of state, the FLASH code uses two of the four adiabatic indexes. One is calculated internally by the FLASH code from the pressure P and internal energy E_{int} using the relation (Fryxell et al., 2000)

$$\gamma = 1 + \frac{P}{\rho E_{\text{int}}}, \quad (2.15)$$

and the other, Γ, must be calculated by the equation of state. By definition (Chandrasekhar, 1957):

$$\Gamma = \left(\frac{\partial \ln P}{\partial \ln \rho}\right)_S \quad (2.16)$$

As described in the previous section, the ACES-EOS constructs an energy-density ACES-EOS table, as required by the hydrodynamical solver in the FLASH code. It is from these tabulated values that we have to calculate Γ numerically. Expression (2.16) contains a partial derivative at constant entropy which cannot be calculated for every single point in the ACES-EOS table. Therefore, we need to derive a new expression for Γ in terms of thermodynamic derivatives at constant density and at constant internal energy.

We can write

$$\begin{aligned} \mathrm{d}P &= \left(\frac{\partial P}{\partial \rho}\right)_S \mathrm{d}\rho + \left(\frac{\partial P}{\partial S}\right)_\rho \mathrm{d}S \\ &= \left(\frac{\partial P}{\partial \rho}\right)_{E_{\text{int}}} \mathrm{d}\rho + \left(\frac{\partial P}{\partial E_{\text{int}}}\right)_\rho \mathrm{d}E_{\text{int}}, \end{aligned} \quad (2.17)$$

and, replacing $\mathrm{d}S$ in equation (2.17) with the following thermodynamic relation (see Mihalas and Mihalas (1984))

$$\mathrm{d}S = \frac{1}{T}\left(\mathrm{d}E_{\text{int}} - \frac{P}{\rho^2}\mathrm{d}\rho\right) \quad (2.18)$$

we have

$$\left(\frac{\partial P}{\partial \rho}\right)_S \mathrm{d}\rho + \left(\frac{\partial P}{\partial S}\right)_\rho \frac{1}{T}\left(\mathrm{d}E_{\mathrm{int}} - \frac{P}{\rho^2}\mathrm{d}\rho\right) = \left(\frac{\partial P}{\partial \rho}\right)_{E_{\mathrm{int}}} \mathrm{d}\rho + \left(\frac{\partial P}{\partial E_{\mathrm{int}}}\right)_\rho \mathrm{d}E_{\mathrm{int}} \tag{2.19}$$

Regrouping the $\mathrm{d}E_{\mathrm{int}}$ and $\mathrm{d}\rho$ terms in the left hand side of equation 2.19 we can derive the following relations

$$\left(\frac{\partial P}{\partial \rho}\right)_S - \frac{P}{T\rho^2}\left(\frac{\partial P}{\partial S}\right)_\rho = \left(\frac{\partial P}{\partial \rho}\right)_{E_{\mathrm{int}}}, \tag{2.20}$$

and

$$\frac{1}{T}\left(\frac{\partial P}{\partial S}\right)_\rho = \left(\frac{\partial P}{\partial E_{\mathrm{int}}}\right)_\rho \tag{2.21}$$

Multiplying equation (2.20) by P/ρ and using equation (2.21) in equation (2.20) to replace the $(\partial P/\partial S)_\rho$ term we obtain:

$$\frac{\rho}{P}\left(\frac{\partial P}{\partial \rho}\right)_S - \frac{1}{\rho}\left(\frac{\partial P}{\partial E_{\mathrm{int}}}\right)_\rho = \frac{\rho}{P}\left(\frac{\partial P}{\partial \rho}\right)_{E_{\mathrm{int}}}. \tag{2.22}$$

Finally, reorganizing equation (2.22) and using the definition of Γ given by equation (2.16), we can express Γ as

$$\Gamma = \frac{\rho}{P}\left(\frac{\partial P}{\partial \rho}\right)_{E_{\mathrm{int}}} + \frac{1}{\rho}\left(\frac{\partial P}{\partial E_{\mathrm{int}}}\right)_\rho \tag{2.23}$$

The final expression for Γ given by equation (2.23) only contains derivatives at fixed density and fixed internal energy. These partial derivatives are easily calculated for all the points in the energy-density table provided by the ACES-EOS. The calculated Γ values are stored by the ACES-EOS sub-unit in the FLASH code, and are used by the hydrodynamical solver.

2.3.3 ACES-EOS and Γ Tests

Before we can use the ACES-EOS sub-unit that we implemented in the FLASH code, it is important to perform some tests. First, we have to make sure that the energy-density ACES table is constructed correctly and that the ACES-EOS sub-unit in the FLASH code is reading the ACES-EOS table properly. For that purpose, we use the ACES-EOS module of the PHOENIX code to calculate the internal energy and density for a given temperature and pressure. We then use these obtained internal energy and density as input values in the FLASH code ACES-EOS sub-unit, which reads the ACES-EOS table and determines the corresponding temperature and pressure. The temperature and pressure values obtained correspond to the initial values used in

the PHOENIX ACES-EOS module, and that proves that the ACES-EOS energy density table is correctly constructed and properly read by the FLASH code ACES-EOS sub-unit.

Second, we need to verify that the internal energy and the entropy values calculated by the ACES-EOS are correct. One way to do this is to calculate the adiabatic index Γ using expressions (2.23) and (2.16). The Γ calculated using equation (2.16) depends on the entropy value but not on the internal energy value, whereas the Γ calculated using equation (2.23) depends on the internal energy but not on the entropy. As mentioned before, the partial derivatives at fixed density and fixed internal energy are easily calculated from the ACES-EOS energy-density table. To calculate the partial derivative at constant entropy required by equation (2.16), we construct a density-entropy ACES table. Figure 2.4 shows that the values of Γ calculated using the two different expressions (2.23) and (2.16) agree reasonably well. Since one expression only depends on the internal energy and the other depends only on the entropy, the fact that both produce the same results suggests that the values of internal energy and entropy calculated by the ACES-EOS are correct.

One could argue that the above result is not conclusive enough since the expressions for the calculation of the internal energy and the entropy both contain a term that depends on the partition function (see equations (2.12) and (2.14)). Therefore, an error in the partition function would result in an error in both the entropy and the internal energy and could result in the calculated values of Γ being both wrong but similar. So, as an example of how sensitive the Γ values are to errors in the energy calculation, we construct an ACES-EOS table with wrong internal energy values, that do not take into account the dissociation energy of the molecules. We calculate again the adiabatic index Γ using both expressions (2.12) and (2.14) and the incorrect ACES-EOS table. We plot these Γ values and compare them with those obtained when using the correct ACES-EOS. In Figure 2.5 we can see that, when using the incorrect ACES-EOS table, the Γ calculated using expression (2.12) differs greatly from the Γ calculated using the expression (2.14). It also differs from the values of Γ calculated using the correct ACES-EOS table. This result further confirms that the values of the energy and the entropy calculated by the ACES-EOS are correct.

Finally, the Γ-values plotted in Figure 2.4 agree with those calculated by Dorfi (1998) for a simpler Hydrogen-Helium equation of state. This agreement validates the internal energy and entropy values calculated by the ACES-EOS. Additionally, Dorfi (1998) asserts that the minimum in the Γ plot between 2000K and 4000K is due to the dissociation of H_2 molecules. This explains why there is a bump in the Γ-values (see Figure 2.5) if the molecular dissociation energy is not included in the ACES-EOS table.

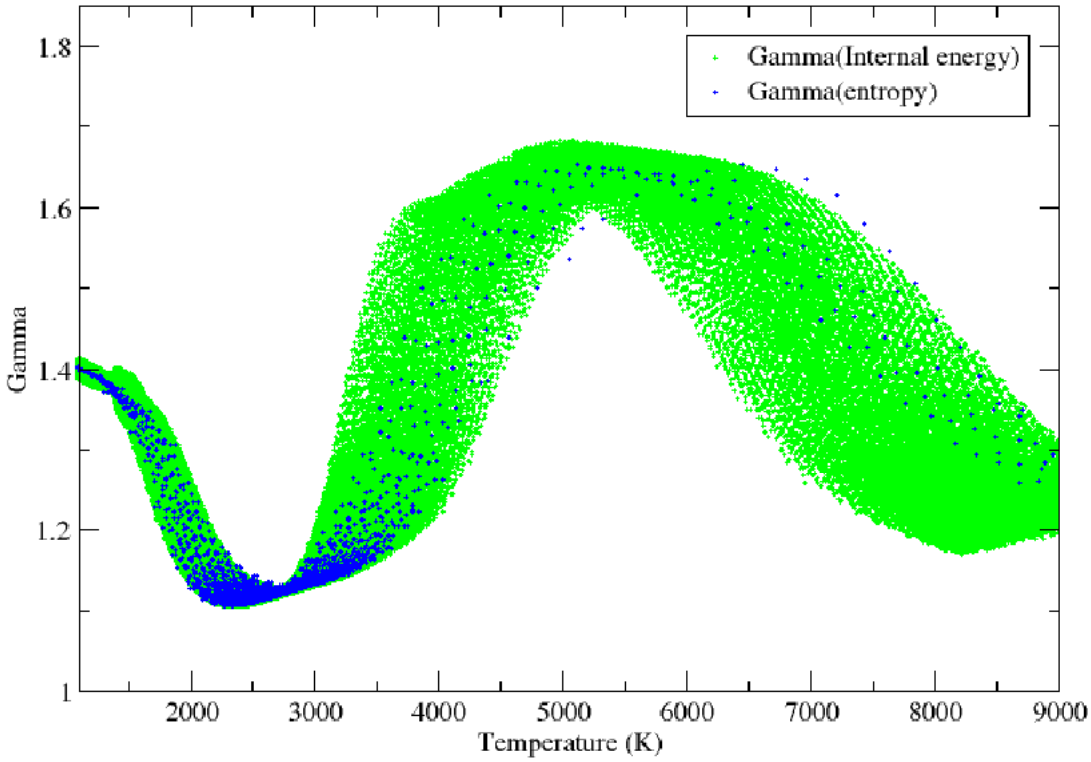

Figure 2.4: Values of Γ calculated using equation (2.23) (green dots) and equation (2.16) (blue dots) as a function of temperature and for densities $8e-9 < \rho < 4e-7$.

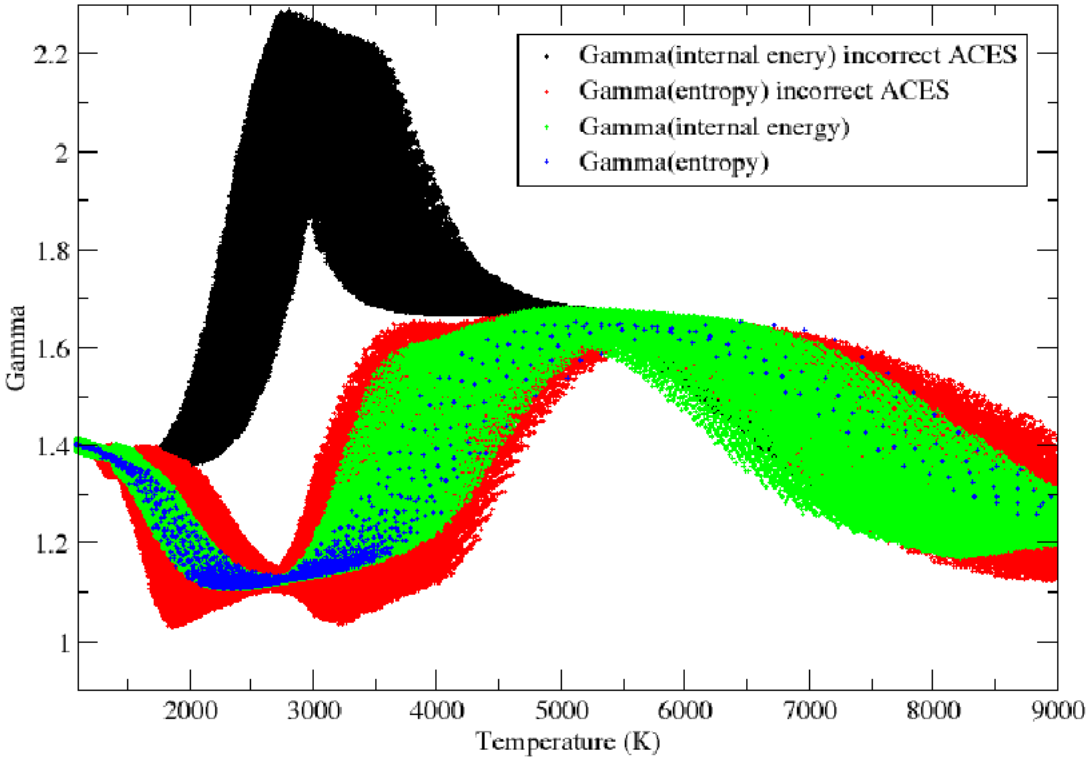

Figure 2.5: Values of Γ as a function of temperature and for densities $8e-9 < \rho < 4e-7$, calculated using two different ACES-EOS tables, one with correct values and one with incorrect values of the internal energy. The Gamma values calculated using the correct ACES-EOS are depicted by the green dots when we use equation (2.23) and by the blue dots when we use equation (2.16). For the case of the incorrect ACES-EOS table, the black dots represent the Γ calculated using equation (2.23), and the red dots are obtained using equation (2.16).

Chapter 3

Simulation setup

3.1 The simulation domain: A box in the star or a star in a box?

As it often happens in Astrophysics, the typical spatial scales of our problem cover a wide range. On one hand, since we want to simulate convection explicitly, the simulations should ideally resolve even the smallest turbulent features. On the other hand, since the global circulation of the gas can influence the local convective structure, we should ideally simulate the whole object. The radius of a given sub-stellar object can be determined, for example, from evolutionary models and, although convection happens on many spatial scales, it is common to define a typical size of the convective cells. This typical size is of the order of the pressure scale height H_p. For an object in hydrostatic equilibrium, the pressure scale height can be obtained from the pressure, density and gravity using (Kippenhahn and Weigert, 1991),

$$H_\mathrm{p} = \frac{P}{\rho g} \tag{3.1}$$

Here, we consider the case of an M-dwarf with effective temperature $T_\mathrm{eff} = 2800$K and gravity $\log(g) = 5$ in cgs units and with a radius of around 1.15×10^5km. In the simulation setup process, we use a PHOENIX/1D model (S. Witte, private communication) for these given effective temperature and gravity. This model is calculated using the PHOENIX Code (Hauschildt and Baron, 2011) and provides the temperature, pressure and density structure of the outermost layers of such an object. From these PHOENIX/1D density and pressure structures, we can calculate the pressure scale height for a given altitude using equation (3.1). At the top of the convective layer this pressure scale height is $H_\mathrm{p} = 12.3$km. At the bottom of the PHOENIX/1D model, still within the convective layer and around 180km below its top, the pressure scale height is $H_\mathrm{p} = 49$km.

These simple pressure scale height estimations clearly show that the radius of the object

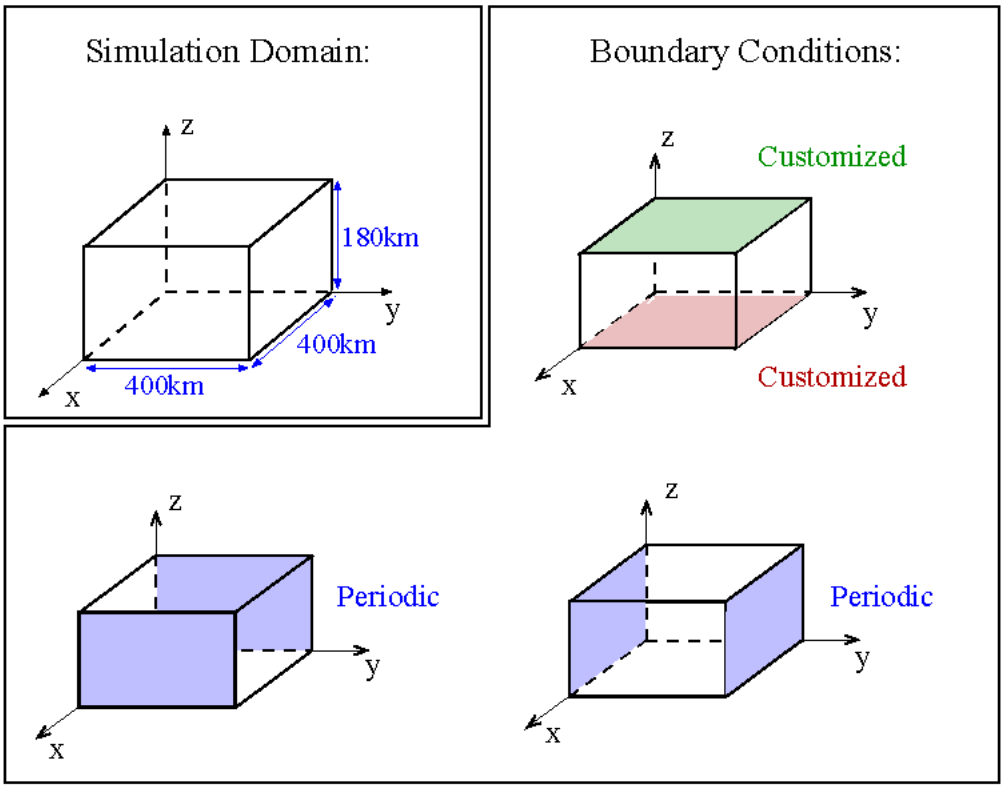

Figure 3.1: The simulation domain consists of a 3 dimensional box embedded in the upper part of the convective region of the sub-stellar object. The size of the box depends on the effective temperature and surface gravity. The boundary conditions are periodic in x and y and for the z direction specially modified boundary conditions were constructed.

is four orders of magnitude larger than the size of the convective features we want to study. Taking into account that we would need a resolution at least one order of magnitude smaller than the typical size of the convective features to resolve them, and considering that we are dealing with a 3D problem, it is not feasible to simulate global circulation and local convection simultaneously. We focus therefore on the explicit simulation of convection and do a local 3D simulation of a region in the upper part of the convective layer. This simulation box (shown in the upper left corner of figure 3.1) is 400km$\times$400km$\times$180km, is several times bigger than the estimated H_p, so that it can contain a reasonable number of convective cells. Its resolution is $160 \times 160 \times 80$ grid points, which corresponds to grid cells' sizes of 2.5km in the x and y directions and 2.25km in the z direction.

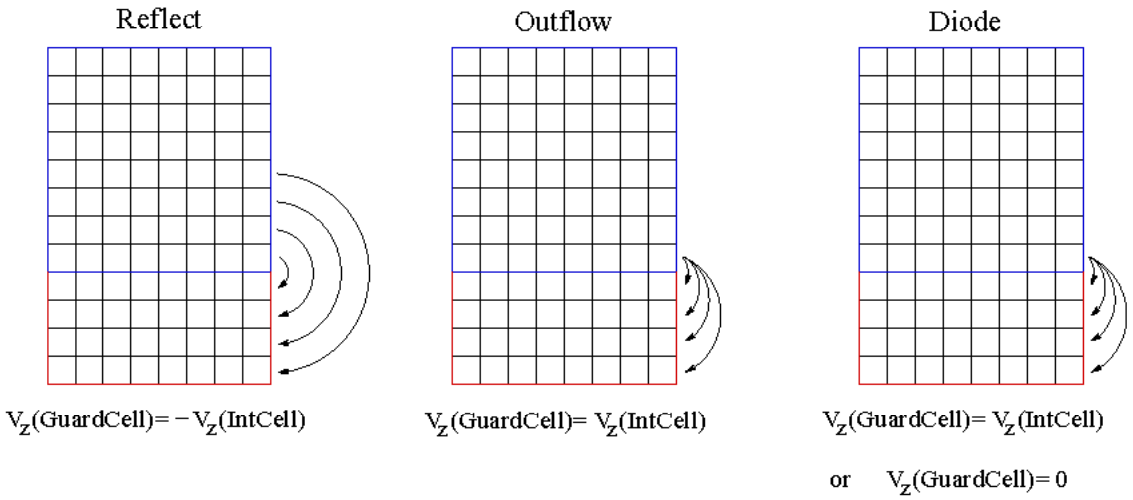

Figure 3.2: The tree panels show schematically how the data in the guard cells (framed by the red lines) is copied from the interior cells (framed by the blue lines) for the tree different boundary conditions provided by the FLASH code: the "reflect", "diode" and "outflow" boundary conditions.

3.2 Boundary conditions

Once the size of the simulation box is established, we need to decide upon its physical location within the object. It is important to mention here that the FLASH code does not handle radiative processes. Therefore, we can only simulate regions where radiation plays a negligible role in the total energy transport, restricting the location of the simulation domain to the the purely convective region. As a result, the choice of the boundary conditions becomes a crucial step in the simulation setup process. The obvious choice for the lateral boundary conditions (x and y in figure 3.1) is periodic boundaries. The choice of the upper and lower boundary conditions is not as straight forward and requires some extra considerations. But before we can discuss in detail these requirements, it is important to understand how the FLASH code handles the boundary conditions.

The boundary conditions provided by the FLASH code are "periodic", "outflow", "diode" and "reflect". As described in Section 2.1, the simulation domain in the FLASH code is divided into blocks that are further subdivided into grid cells. Each block is surrounded by guard cells, and if a block lies at a boundary, its boundary guard cells are filled according to the chosen boundary condition. The values of velocity, density, pressure, temperature and energy in the guard-cells are copied from the interior cells. Figure 3.2 shows schematically how that is done

for each type of boundary condition. For the "reflect" boundary conditions the data is copied in a mirror-like way. Additionally, the sign of the z-component of velocity at the guard cells is changed. As a result no material leaves the simulation domain, and we can think of the boundary as a "rigid" surface where material bounces back into the domain. In the "outflow" and "diode" boundary conditions the data is copied in a way that allows outflows to freely leave the domain, and the only difference between the two boundary types is in the velocity treatment. The "outflow" boundary condition copies the velocity in the same way as the rest of the data, allowing inflows as well as outflows. On the contrary, in the case of the "diode" boundary condition, the velocity is either copied as the rest of the data or set to zero if it is pointing inwards. As a result, the "diode" boundary condition does not allow inflows of material.

The interiors of sub-stellar objects and very low-mass stars are mostly fully convective. So, no matter how deep we place the lower boundary of our simulation, it will always be within the convective region. The upper boundary is also within the convective region, because the FLASH code does not handle radiation. So both the upper and lower boundaries have to allow inflows and outflows of material. With that in mind, the FLASH "outflow" boundary condition seems appropriate. Nevertheless, there is another requirement for the upper and lower boundaries that is related to the values of the temperature, density and pressure. If we look again at how the "outflow" boundary condition fills the guard cells (figure 3.2), we can see that there is no temperature, density or pressure gradient between the interior cell and the guard cells. For an object in hydrostatic equilibrium, the effect of gravity is counteracted by the pressure gradient. But since we have no pressure gradient in the "outflow" boundary condition it is impossible to have equilibrium at the boundaries. The "diode" boundary condition has also zero gradient at the boundaries, and the "reflect" boundary condition does not allow inflows and outflows. Therefore none of the boundary conditions provided by the FLASH code fulfill the requirements of our simulation, and we must construct a customized set of boundary conditions.

As described above, there are two main requirements for the boundary conditions: they must allow inflows and outflows of material and they must provide some sort of gradient to counteract the gravity. To fulfill the first requirement, we use the "outflow" treatment of the velocity for the lower boundary and the "diode" treatment of the velocity for the upper boundary. We do not use the "outflow" treatment in the upper boundary because, due to the low densities, it can result in unrealistic inflows of material which will be discussed later in this work. To fulfill the second requirement, we fix the values of the density, internal energy, temperature and pressure in the upper and lower boundaries. Fixing the value of the internal energy on the lower boundary is also important for convection because it provides a source of energy. These boundary conditions require values for the energy and density in the upper and lower boundaries. In order to get those values we need to resort to existing models, which will be described

in the following section.

3.3 PHOENIX/1D atmosphere models

An isolated object in hydrostatic equilibrium with a given effective temperature and surface gravity, has a unique temperature, density and pressure structure. We use PHOENIX/1D models (provided by S. Witte, private communication) to get these 1D temperature, density and pressure profiles and use them in the simulation setup process. These models are calculated using the PHOENIX Code (Hauschildt and Baron, 2011), which is a general purpose atmosphere code that calculates the temperature structure of an object solving the radiative transfer equation. In the 1D mode, it assumes the object is in hydrostatic equilibrium and for the convective regions, it uses the mixing length theory approximation to calculate the energy transport due to convection. The PHOENIX/1D models provide only a reference value for the energy and density at the boundaries and an initial structure of the system. The hydrodynamics of the system are the calculated by the FLASH code. We use the PHOENIX/1D models of an object with effective temperature $T_{\rm eff} = 2800$K and surface gravity $\log(g) = 5$ (Figure 3.3), to determine the density, pressure and temperature values for the boundary conditions and use the ACES-EOS table to calculate the corresponding internal energy value. The PHOENIX/1D models together with the ACES-EOS are also used to construct a 3D set of initial conditions for the internal energy, density, temperature and pressure.

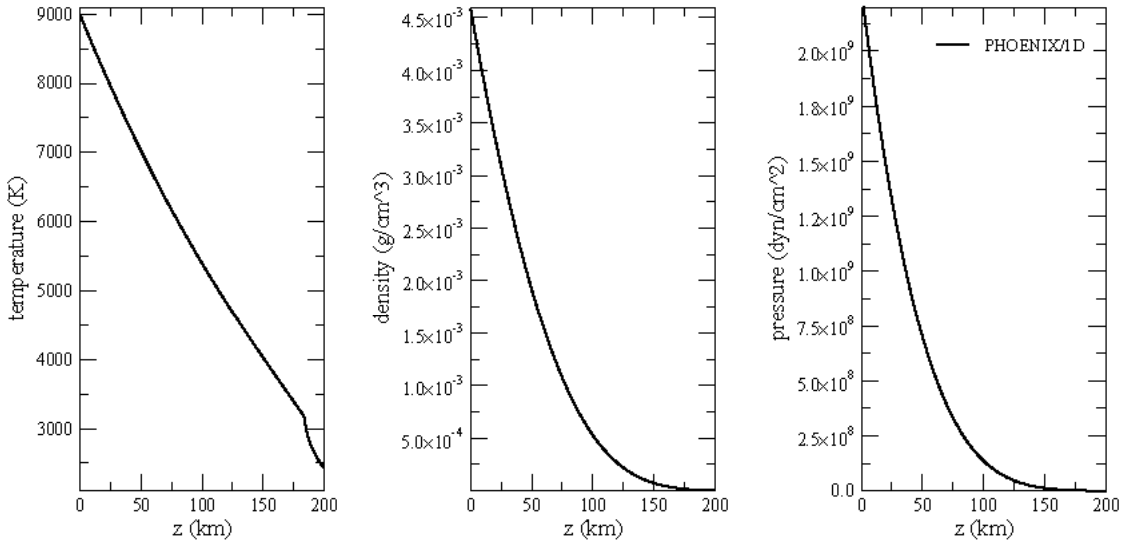

Figure 3.3: 1D temperature, density and pressure vertical profiles of an object with effective temperature $T_{\rm eff} = 2800$K and surface gravity $\log(g) = 5$.

Chapter 4

Results

4.1 Characterizing convection

One of the challenges that we encounter when simulating convection in substellar objects is the verification of the results. Despite being a common phenomenon, direct observations of convection are only possible for objects in our solar system. In the case of the solar system planets (we are particularly interested in giant gaseous planets), the surface structure is dominated by climatic events—due to the solar radiation and the resulting day-side night-side temperature difference—and by rotation. But since we are simulating a section of an isolated object—where we do not consider radiation or rotation—only solar convection can be used as a reference for a qualitative comparison.

A more quantitative validation of the results has to be done using other numerical models. As we described in Section 3.3, the PHOENIX/1D models provide 1D vertical structures that can be used to test the mean vertical profiles resulting from our simulations. In addition to that, the velocities and 3D hydrodynamic structures must be compared to other existing hydrodynamic models. There are several detailed simulations of solar convection (e.g., Stein and Nordlund, 1998) that could be used to validate initial FLASH test simulations. However, one of the main aims of this thesis is to adapt the FLASH code so it can be used to simulate convection in substellar objects, and a crucial step in this process is the coupling of the ACES equation of state to the FLASH code (see Section 2.3). This equation of state handles the chemical processes that occur at low temperatures, and, therefore, has to be tested for objects with lower effective temperatures than that of the sun.

We simulate convection locally, for an object with effective temperature $T_{\rm eff}$=2800 K and surface gravity $\log(g)$=5.0 (in cgs units). This object is an M-dwarf with a mass of around 0.1 solar masses. This mass is slightly larger than the maximum mass for a substellar object (0.075 solar masses). Nevertheless we choose these values of surface gravity and effective temperature in order to be able to compare and validate our results with the 3D models by Wende et al. (2009) and the 2D simulations by Freytag et al. (2010). Once the validation

process is completed, it is straight forward to perform simulations for lower temperatures and lower masses. The simulation domain consists of a 400 km $\times$400 km $\times$160 km box embedded in the upper part of the convective region of the object, with a resolution of $160 \times 160 \times 80$ grid points, which corresponds to grid cells' sizes of 2.5 km in the x and y directions and 2.25 km in the z direction. We use the FLASH code coupled to the ACES-EOS, and use customized boundary conditions in the z direction. The PHOENIX/1D model atmospheres are used to fix the density and internal energy upper and lower boundary values, as well as to construct the initial conditions.

In the following, we analyze the results of the above described simulation, looking for evidences of convection in 2D horizontal and vertical slices of the domain. We then compare the mean 1D vertical structures to the PHOENIX/1D models and test the dependence of the results on the initial and boundary conditions. Based on this analysis, we are able to correct the lower boundary conditions to improve the results, and finally run a higher resolution simulation.

4.1.1 Evidence of convection: looking for a granulation pattern.

In the inactive parts of the solar surface it is possible to see hot rising regions surrounded by colder filaments of sinking material. This convective pattern, also known as solar granulation, has been observed in detail, and simulated extensively (e.g., Stein and Nordlund, 1998). The typical sizes of convective cells depend on the pressure scale height (see Section 3.1), and, as the M-dwarf simulations by Ludwig (2006) show, convective patterns change for objects with effective temperatures lower than that of the sun, and also change if instead of analyzing convection in the surface, we consider deeper layers.

Since we are simulating an object that is cooler and has a bigger surface gravity than the sun, we expect differences in the typical sizes of the convective cells with respect to the solar granulation pattern. It is also important to recall that our simulations do not consider radiation and are limited to the deeper, purely convective regions. As a result, every horizontal slice of our simulation domain corresponds to a sub-surface layer.

Despite the above described differences, we expect some qualitative similarity between our results and the solar granulation pattern. Indeed, in the z-velocity horizontal slices at three different altitudes (left panels Figure 4.1), we can see that granule-like regions of material are moving upwards and are surrounded by filament-like structures of sinking material. It is hard to derive from this figure a typical size of the granule-like up-flows, but we find that the overall z-velocity structure is similar to the granular structure observed in the Sun (Stein and Nordlund, 1998), and is also very similar to the "deeper-layer" slices of the M-dwarf simulations by Ludwig (2006).

Furthermore, if we compare the horizontal z-velocity patterns with the corresponding tem-

perature structures (right panels Figure 4.1) we see that, for $z = 100$km and $z = 130$km, the rising granules are relatively warm and the sinking filaments are relatively cold, as expected in a convective system. This correspondence between temperature and z-velocity structure is not so clear for $z = 50$km. However, this is likely due to a boundary effect that is discussed in Section 4.2.1. We can also note that the temperature variations at a given altitude (shown in Figure 4.1) are smaller compared to the total temperature range (from top to bottom of the domain) and are therefore not visible in the 2D vertical temperature slice (see right panel Figure 4.2).

In addition to the evidence of convection observed in the horizontal slices at different altitudes (Figure 4.1), we also see up-flows and down-flows of material consistent with convection in a 2D vertical slice of the simulation domain (left panel Figure 4.2). All the z-velocity and temperature slices of the simulation domain exhibit evidences of convection. Warmer regions rise while colder regions sink. In the following Section we seek to quantify these results by studying in more detail the correlation between the z-velocities and the main thermodynamical quantities.

4.1.2 Up-flows, down-flows and their correlation with temperature and density.

Convection is characterized by up-flows of relatively warm and less dense material and down-flows of relatively cold and denser material. Therefore, it is the relative value of temperature, density and pressure that is relevant for characterizing convective motions. We compute these relative values, or anomalies, as the value at a point minus the average value at that altitude. We then divide the result by the average value at that altitude, to express the anomalies as a fraction of the horizontal average. To confirm that the up and down-flows observed in Figure 4.2 correspond to convective motions, we plot in Figure 4.3 the temperature, density and pressure anomalies overlapping the contours of the z-velocity field.

The strong temperature anomalies observed in the lower part of the domain (upper panel Figure 4.3) are likely due to a boundary effect, since they exist only close to the lower boundary. The density anomalies (middle panel Figure 4.3) are also stronger in the lower part of the simulation domain. We treat these anomalies that are close to the lower boundary as pure boundary effects (for further justification see Section 4.2.1), and concentrate instead on the middle region of the simulation domain.

In this middle region (between $z = 50$km and $z = 120$km) there is a clear correspondence between the warmer regions and the up-flows and the colder regions and the down-flows (upper panel Figure 4.3). Despite the high variability in the density anomalies plots, we also see that the up-flows of material have in average smaller densities and the down-flows of material have larger densities (middle panel Figure 4.3). This correspondence between the warmer-less dense

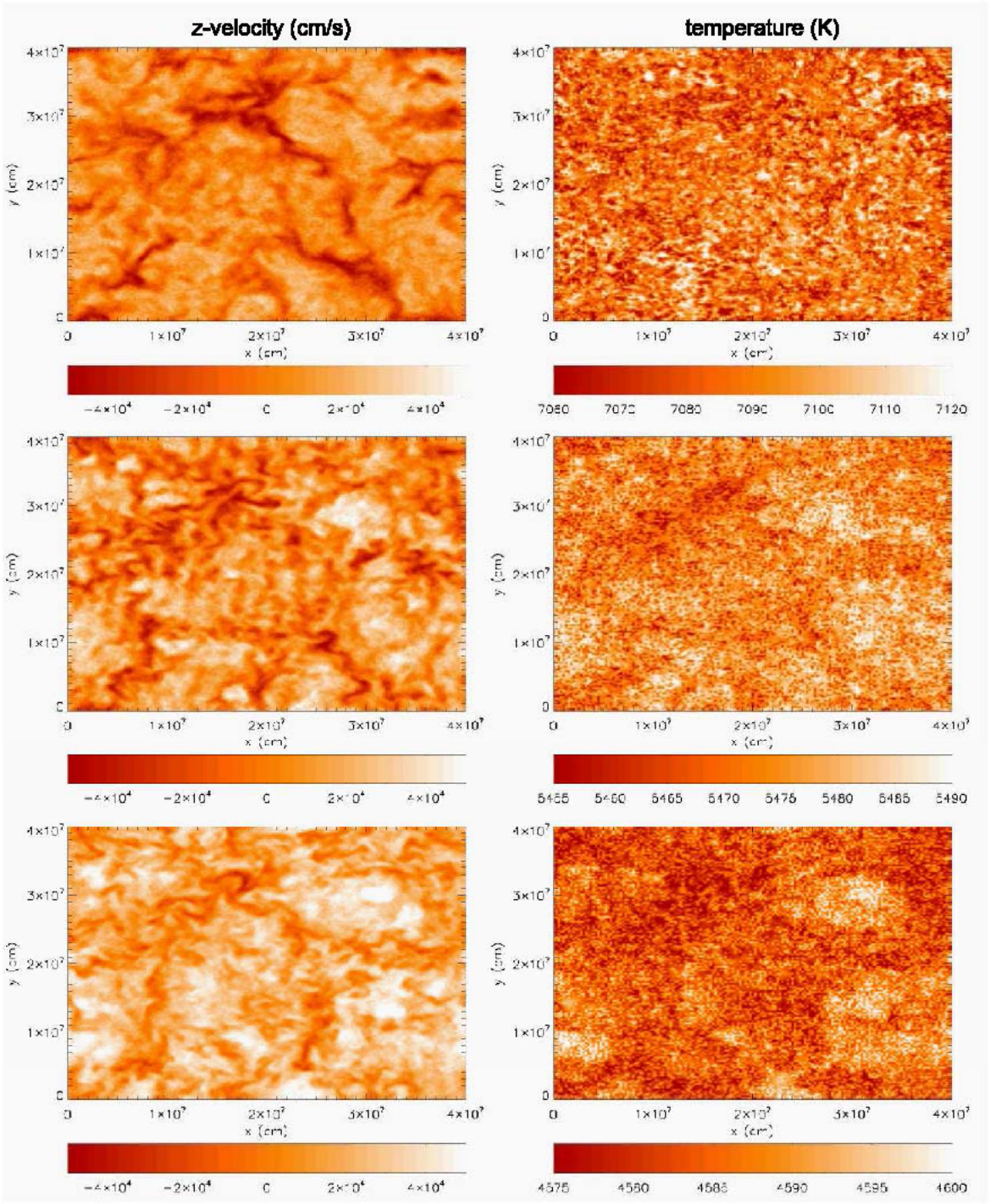

Figure 4.1: Horizontal slices of the z-velocity structure (left panels) and the temperature structures (right panels) at three different heights: $z = 50$km (upper panels), $z = 100$km (middle panels) and $z = 130$km (lower panels), where $z = 0$km corresponds to the lower boundary and $z = 180$km corresponds the upper boundary. In the z-velocity plots (left panels), the brighter regions correspond to up-flows of material and the darker filaments correspond to down-flows. In the temperature plots (right panels) the brighter regions correspond to warmer regions and the darker regions correspond to colder regions. This structures correspond to simulations of an object with $T_{\rm eff} = 2800$ K and $\log(g) = 5.0$.

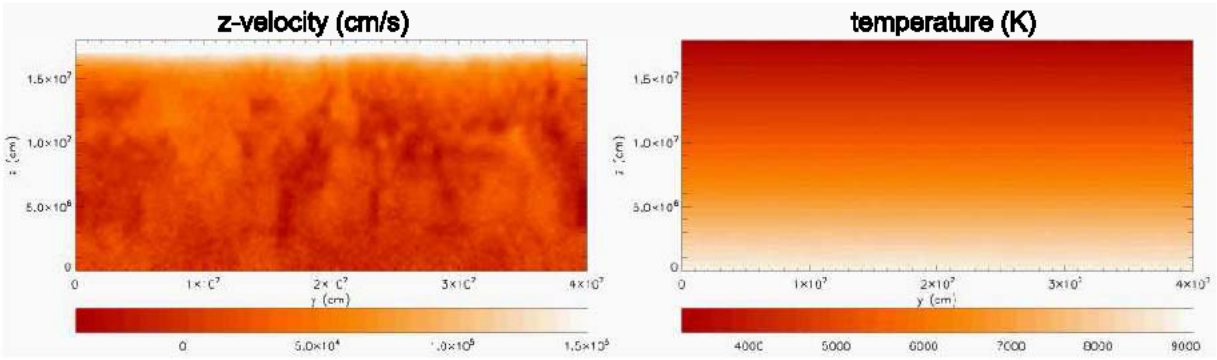

Figure 4.2: Vertical 2D slices of z-velocity (left panel) and temperature (right panel) of an object with $T_{\rm eff} = 2800\,{\rm K}$ and $\log(g) = 5.0$. In the z-velocity profile (left panel) the brighter regions correspond to up-flows of material and the darker filaments correspond to down-flows.

regions and the up-flows, and between the colder-denser regions and the down-flows is a strong indication of convection. Additionally, in the idealized description of convection (see Section 1.2), we assumed that a parcel of gas rising through a convectively unstable region is in pressure equilibrium with its surroundings. Consistent with this assumption, there is no visual evidence of a correspondence between the pressure anomalies and the z-velocity (lower panel of Figure 4.3). The correspondence (or lack of correspondence) between the vertical velocity and the temperature, density and pressure anomalies are all consistent with convective motions.

A correlation analysis between the different variables allows us to verify in a more rigorous way the existence of convective motions. The upper panels of Figure 4.4, reveal that there is a clear correlation between the temperature anomalies and the z-velocity, with warmer regions going upwards and colder regions moving downwards. For the density anomalies, the correlation with the z-velocity is less evident than for the temperature anomalies (middle panels in Figure 4.4). There is a bigger spread in the data, but the linear regression shows consistently for the three different altitudes that there is an anticorrelation, with the denser regions sinking while the less dense regions rise. Finally, the pressure anomalies also seem to be slightly correlated to the z-velocity (lower panels Figure 4.4). The correlation coefficients (Table 4.1) and the slope of the linear regressions corroborate the above described results.

4.1.3 Vertical profiles and comparison to PHOENIX/1D models

In the analysis of the z-velocity field and its correlation with temperature and pressure anomalies, there is a strong evidence of convection (Figure 4.3), further supported by the hori-

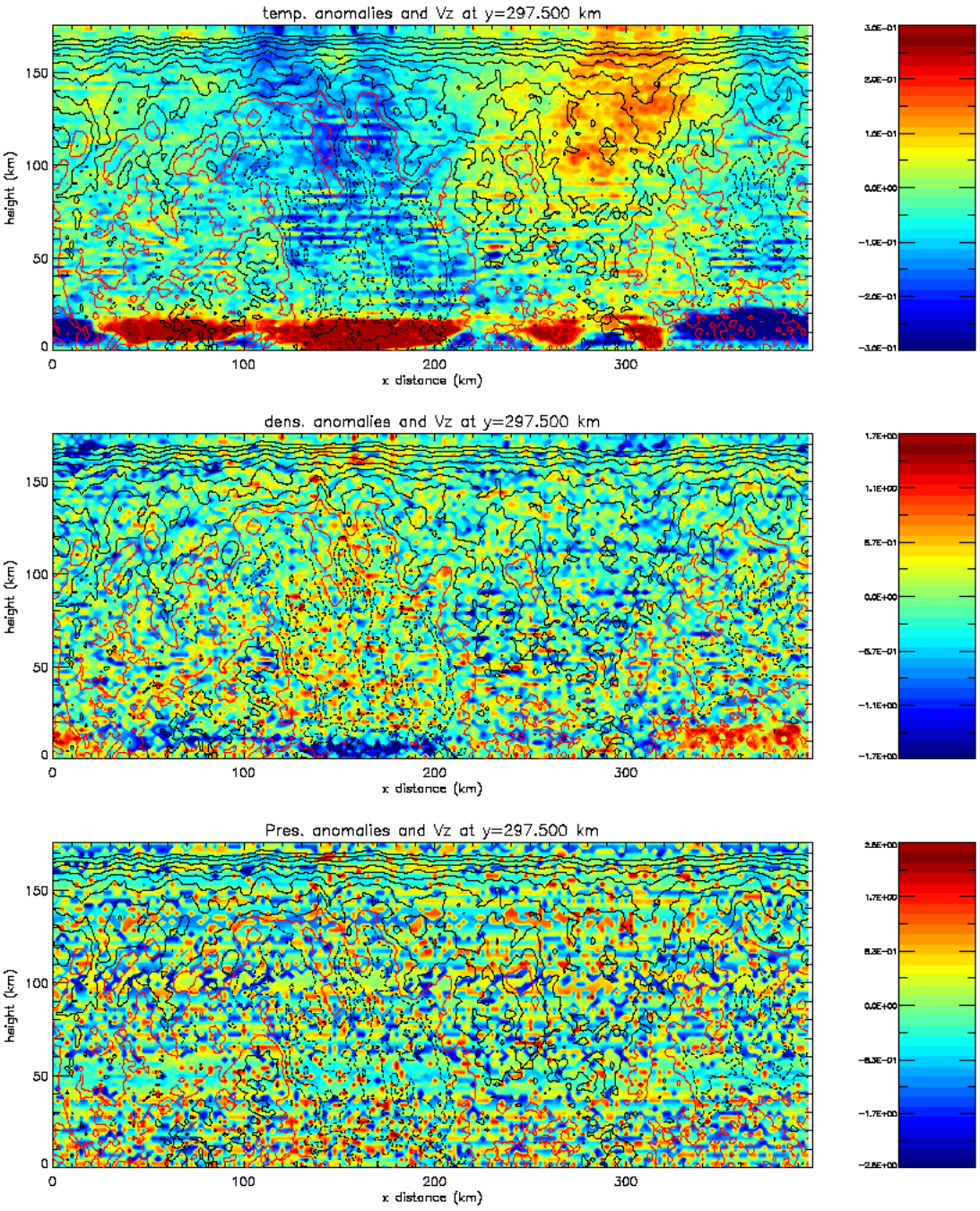

Figure 4.3: 2D vertical slices of the temperature (upper panel), density (middle panel) and pressure (lower panel) anomalies, for an object with $T_{\rm eff} = 2800$ K and $\log(g) = 5.0$. These anomalies are given as a percentage of the horizontal average value. The isocontours of the z-velocity field are plotted overlapping the temperature, density and pressure anomalies, with the isocontour of the zero z-velocity plotted in red, the negative z-velocities plotted in black dashed lines and the positive z-velocities plotted in continuous black lines.

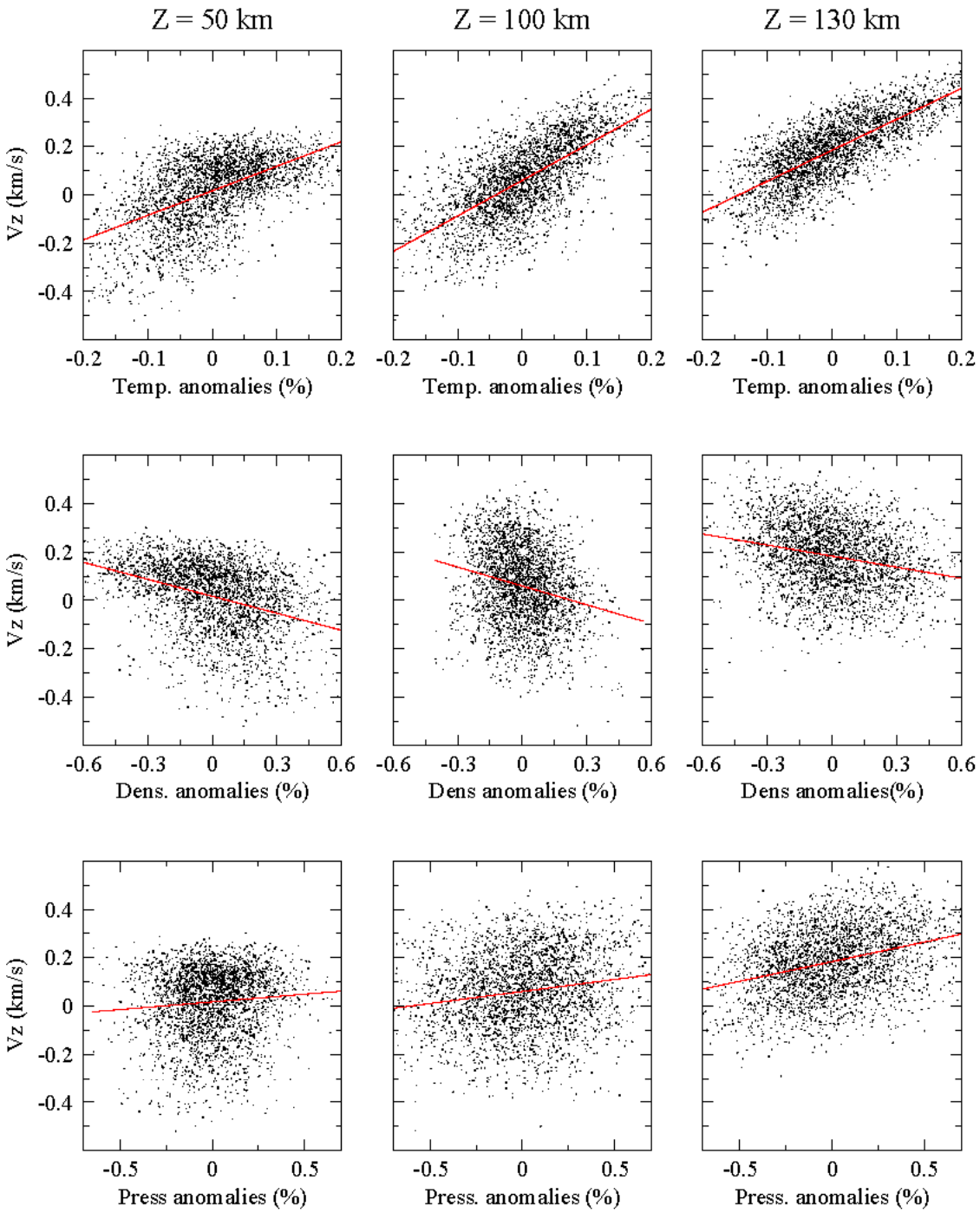

Figure 4.4: Scatter plots of temperature (upper row), density (middle row) and pressure (lower row) anomalies, against the vertical velocity at $z = 50$km (left column), $z = 100$km (middle column) and $z = 130$km (right column). Each point corresponds to an average of $3\times34\times3$ gird cells. The red line corresponds to a linear regression of the data.

	slope (km/s)	intercept (km/s)	correlation coefficient
temp 50km	1.015	0.017	0.559
dens 50km	-0.234	0.017	-0.375
pres 50km	0.064	0.017	0.088
temp 100km	1.469	0.060	0.677
dens 100km	-0.260	0.060	-0.223
pres 100km	0.099	0.060	0.177
temp 130km	1.277	0.184	0.765
dens 130km	-0.152	0.183	-0.246
pres 130km	0.162	0.184	0.340

Table 4.1: Correlation coefficients and linear regression parameters corresponding to the scatter plots in Figure 4.4.

zontal slices of the simulation domain that show a granular structure qualitatively similar to that observed in the solar surface (Figure 4.1). Nevertheless, in addition to these qualitative comparisons to the solar granulation pattern, we also need to verify that the simulated structures are quantitatively correct. In order to do so, we make horizontal averages of temperature, density and pressure and compare these resulting FLASH 1D-averaged vertical profiles with the PHOENIX/1D models (described in Section 3.3). In Figure 4.5 we can see that there is a very good general agreement between the two models. The FLASH density and pressure structures reproduce very well the PHOENIX/1D models, which is an indication that the FLASH simulation is in hydrostatic equilibrium (or at least very close to hydrostatic equilibrium). There is also a very good agreement between the temperature structures of the two models. Since we simulate a region where convection is the main energy transport mechanism, and considering that the temperature structure is determined by the energy structure, we can conclude that the convective energy transport is correctly reproduced in the FLASH model.

However, a zoom of the central region of the simulation domain (Figure 4.6) shows that the FLASH temperature profile is slightly shifted with respect to the PHOENIX/1D model. Nevertheless, this shift to higher temperatures does not change the temperature gradient, which indicates that the energy transport, and therefore convection, is not responsible for this shift. There are two possibilities to explain the temperature shift: one is that there is a systematic error when we associate the temperature value to the center of the grid cell (when in fact the temperature value is a grid-cell-average and is not necessarily associated with any particular point in space, as described in Section 2.2). The second option is that the energy value that we use for the lower boundary is also slightly shifted. This second option is analyzed and discussed in Section 4.2.2.

Despite the slight shift in the FLASH temperature structure with respect to the PHOENIX/1D

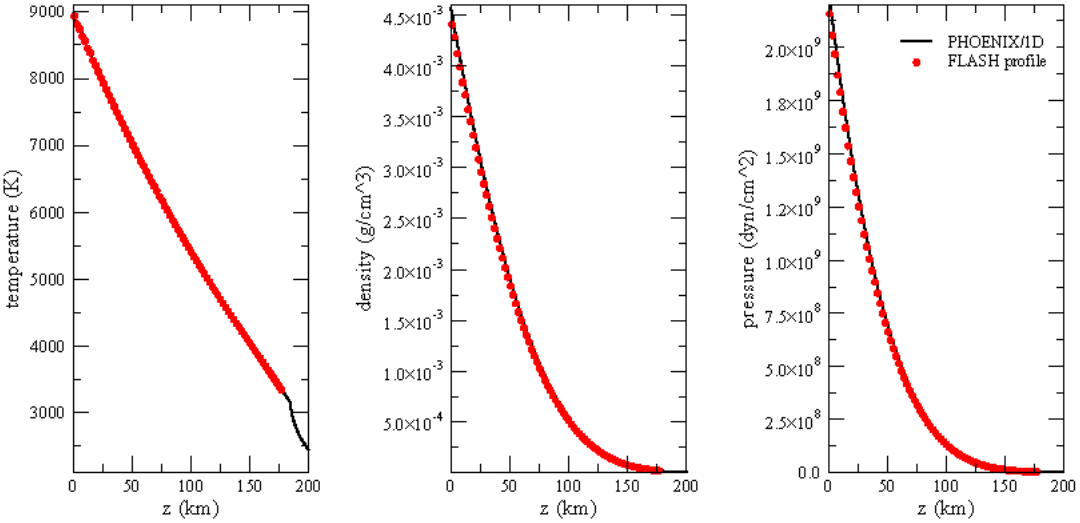

Figure 4.5: Temperature, density and pressure profiles for the 1D-averaged FLASH results (in red dots) and for the PHOENIX/1D models (in black).

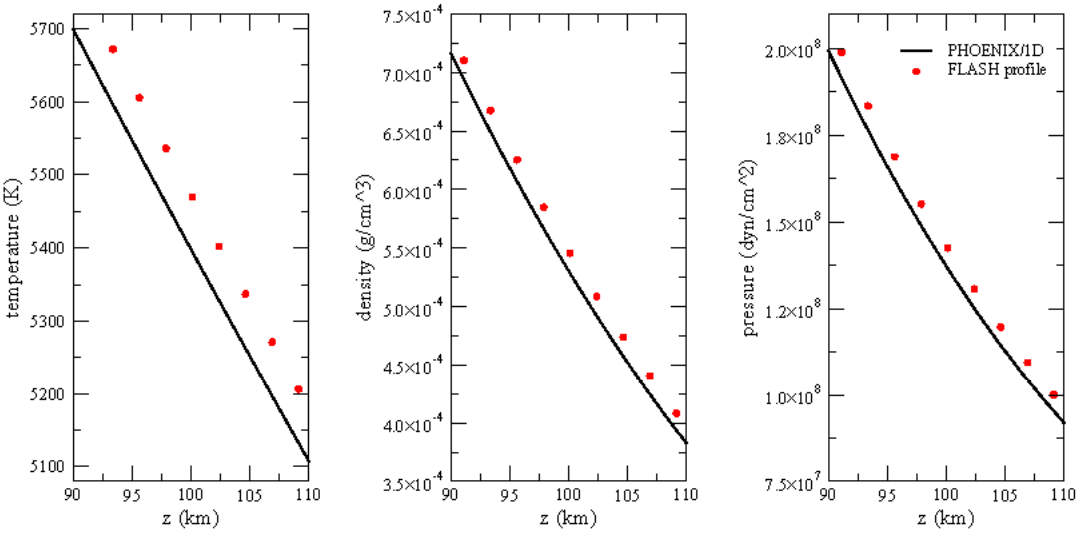

Figure 4.6: Zoomed-in view of the temperature, density and pressure profiles for the 1D-averaged FLASH results (in red dots) and for the PHOENIX/1D models (in black).

model, we can conclude that there is in general a very good agreement between the FLASH 1D-averaged-profiles and the PHOENIX/1D models. It is important to keep in mind that the PHOENIX/1D and the FLASH models calculate the resulting temperature, density and pressure 1D structures in independent and complementary ways: the PHOENIX code solves the non-grey radiative transfer equation and uses the mixing lenght theory approximation for the convective energy transport and the FLASH code solves the hydrodynamic equations and does not take into account radiation. Therefore, the good agreement between the two models observed in Figure 4.5 provides a good validation of the FLASH results at large depths. However, despite the fact that the two models are calculated using different codes and by solving a different set of equations, the two models are linked: the FLASH code uses the PHOENIX/1D models to construct the boundary conditions and the initial conditions. We can argue that the FLASH results should be independent of the initial conditions and that the use of PHOENIX/1D values in the lower boundary is only a tool to ensure that we simulate the same object with the two different codes, so that we can later compare the results. These arguments justifying the independence of the two models are tested in Section 4.2.

4.1.4 Vertical velocity analysis

From the above analysis of the results we conclude that the FLASH simulations reproduce correctly the temperature, density and pressure structures. We also observe a granular-like pattern in the z-velocity field and a correlation between the z-velocities and the temperature and density anomalies. However, in the upper part of the domain, the z-velocity is predominantly positive and there are no signs of down-drafts (Figures 4.2 and 4.3). This behavior of the z-velocity field is in contradiction with what we expect in a convective region. In such a region, up-flows and down-flows of material coexist at any given altitude and one would expect the average of the vertical velocity to be close to zero. Nevertheless, what we observe in the left panel of Figure 4.7, is that the horizontal averages of the z-velocity are close to zero only in the lower and middle regions of the domain, and that for an altitude $z > 130$km, these averaged z-velocities show a steep increase. The same behavior is observed in the rms z-velocity (middle panel in Figure 4.7), with reasonable values in the lower and middle parts of the domain and an increase in the upper part. We attribute this unexpected behavior of the velocity in the upper part of the domain to a boundary effect, and tests and a resulting improvement to the z-velocity profiles are shown in sections 4.2 and 4.3, respectively. The reasonable rms z-velocity values in the middle and lower part of the domain are of around 0.2 km/s, very similar to the values obtained by Wende et al. (2009) and by Freytag et al. (2010).

Both the z-velocity horizontal averages and the rms z-velocities show an unexpected increase in the upper part of the domain and a reasonable behavior in the middle and lower regions. Nonetheless this reasonable behavior has to be tested further, because in a convective

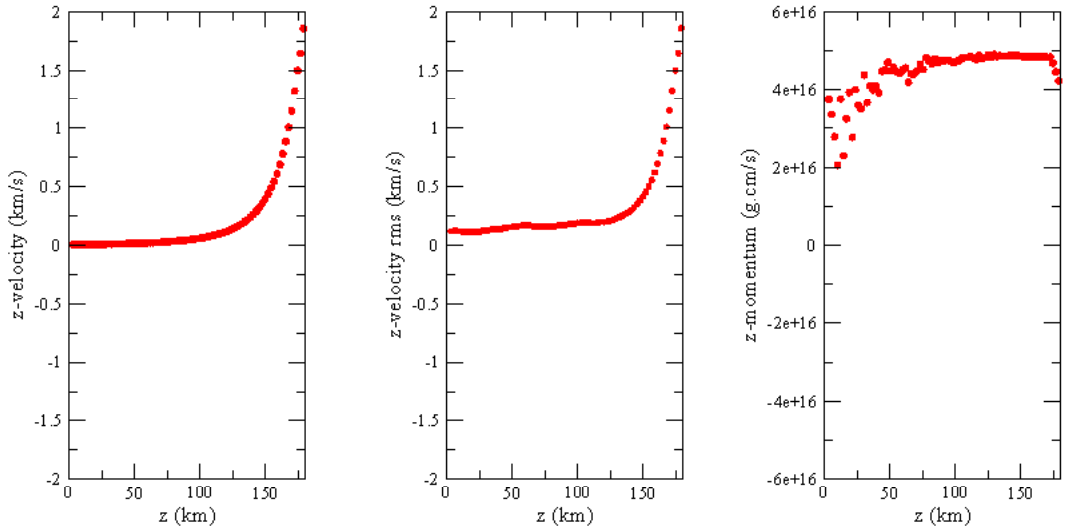

Figure 4.7: Horizontal averages of the z-velocity (left panel), rms z-velocity (middle panel) and horizontal average of the z-component of the momentum (right panel) as a function of altitude.

region the up-flows and down-flows of material have different densities and, as a result, an analysis of the z-velocities can be insufficient. To include density information, we calculate the horizontal average of the z-momentum. In the right panel of Figure 4.7 we can see that the horizontally-averaged z-momentum of the system is almost constant (but not zero) for the middle and upper regions of the simulation domain. The fact that the average z-momentum is not zero implies that there is a net flow of material, which is an indication that the simulations are not in equilibrium. We know that the hydrostatic equilibrium of a system requires that, for a given density, the effect of the gravity is counteracted by the pressure gradient. In our simulations, the pressure gradient is determined by the density and energy values that we use in the lower boundary condition (see section 4.2.2) and therefore, a positive net z-momentum is consistent with an internal energy excess in the lower boundary.

4.2 Impact of the inital and boundary conditions

As seen in Figure 4.5, there is a very good agreement between the FLASH 1D-averaged-profiles and the PHOENIX/1D models. Still, we have to take a few precautions when comparing the FLASH results to the PHOENIX/1D models. As described in Section 3.3, the PHOENIX/1D models are used in the FLASH simulation setup procces, both to get the values of the energy and density at the boundaries and to generate the initial conditions. So it is relevant to determine how much the FLASH results depend on this use of the PHOENIX/1D models. In the following, we will refer to the simulation described in Section 4.1 as the *default*

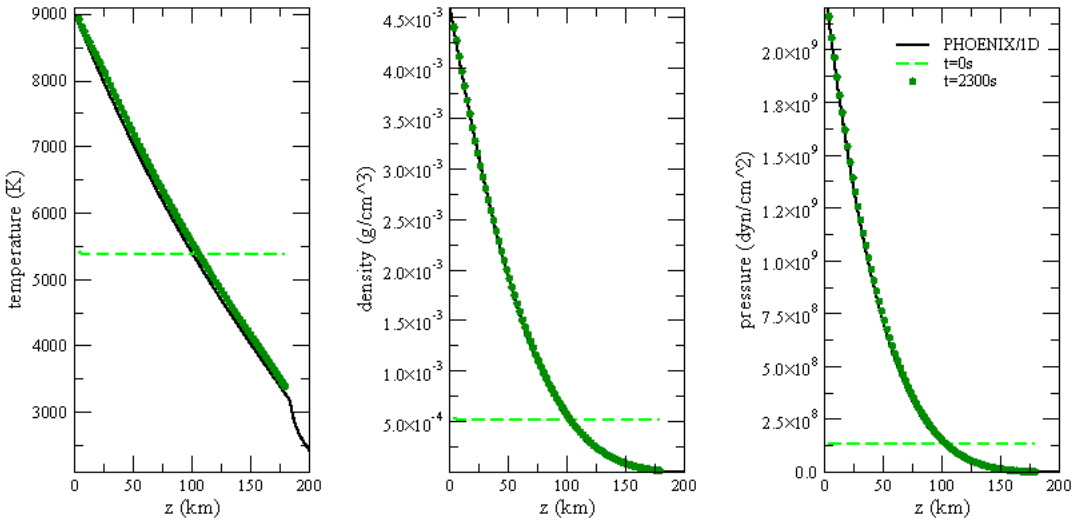

Figure 4.8: 1D-averaged FLASH temperature, density and pressure profiles. The green dashed lines represent the constant profiles used as initial conditions and the green dots represent the resulting 1D-averaged FLASH temperature, density and pressure profiles. The PHOENIX/1D models are again used as a reference (black lines).

simulation, and use it as a reference for this section's initial-conditions, simulation-setup and boundary-condition tests.

4.2.1 Initial conditions and different box sizes

As a first test, we construct a set of initial conditions with constant temperature, density, internal energy and pressure values throughout the domain. To test if the results depend on these "constant initial conditions", we use them to run a simulation with the same runtime parameters and boundary conditions values as the *default simulation*. In Figure 4.8 we see that the resulting FLASH 1D-averaged-profiles fit very well the PHOENIX/1D models, despite starting at constant values. The resulting temperature anomalies and z-velocity field are both very similar to those of the *default simulation* (Figure 4.9). So we conclude that the FLASH results are independent of the initial conditions.

As a second test, we construct a 100km high *smaller box* simulation (instead of the 180km high *default simulation*). We locate this simulation box in the middle of the original domain (see Figure 4.11). The internal energy and density values for the boundary conditions at the new z location are again obtained using the PHOENIX/1D models. We calculate horizontal averages and construct 1D-average profiles corresponding to the *smaller box* simulation. In Figure 4.10 we find that the resulting FLASH 1D-averaged vertical profiles fit very well the PHOENIX/1D models and the FLASH 1D-averaged vertical profiles corresponding to the default simulation. We can conclude that the 1D-averaged-profiles are independent of the size of

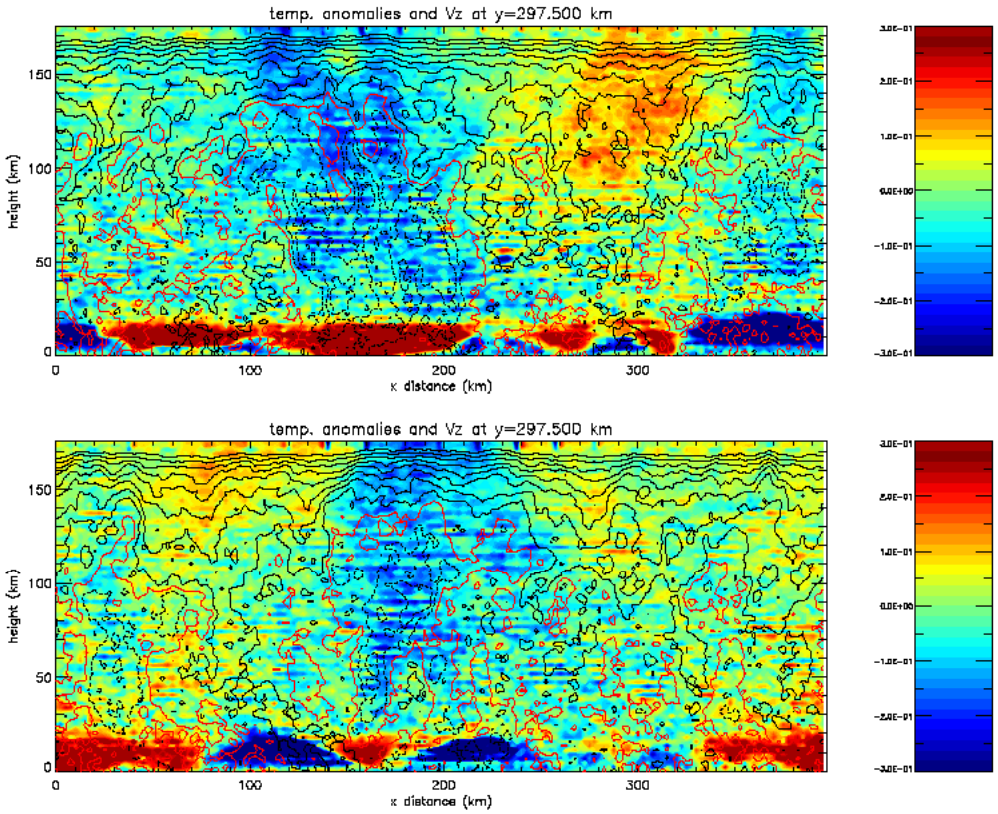

Figure 4.9: 2D vertical slices of the temperature anomalies for the *default simulation* (upper panel) and for the simulation with constant initial conditions (lower panel). These anomalies are given as a percentage of the horizontal average value. The isocontours of the z-velocity field are plotted overlapping the temperature anomalies, with the isocontour of the zero z-velocity plotted in red, the negative z-velocities plotted in black dashed lines and the positive z-velocities plotted in continuous black lines.

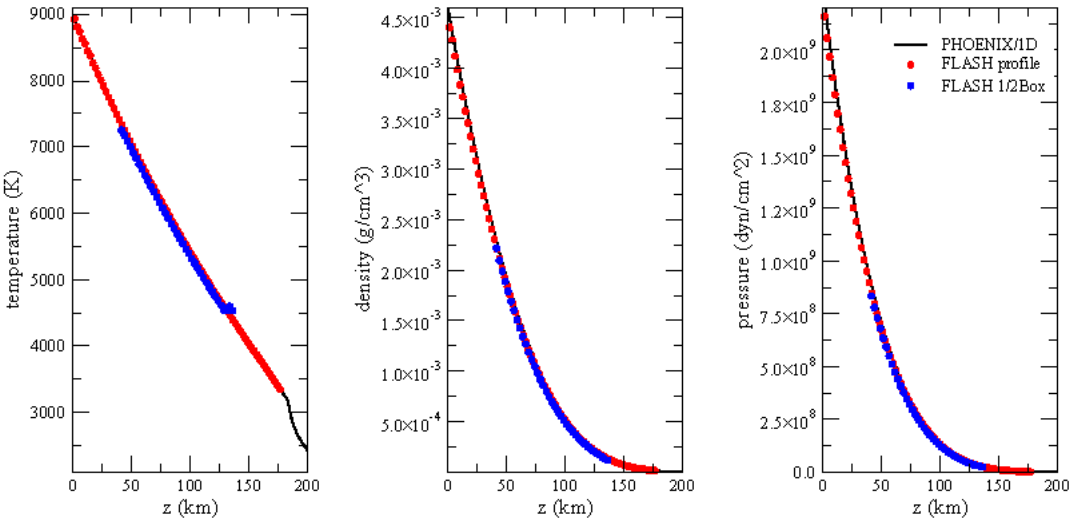

Figure 4.10: FLASH 1D-averaged vertical temperature (left panel), density (middle panel) and pressure (right panel) profiles for the 100km high setup (in blue dots). The 1D-averaged FLASH temperature, density and pressure profiles (in red dots) and the PHOENIX/1D models (in black) are shown as a reference.

the simulation domain, at least for a decrease in hight of up to 40%.

For the *smaller box* simulation, we calculate the temperature, density and pressure anomalies (as described in Section 4.1.2) and compare them to the anomalies of the *default simulation*. Regarding the temperature anomalies and the z-velocities, we see in Figure 4.11 that there are significant differences between the 2D slice plot of the temperature anomalies corresponding to the *smaller box* simulation and the plot corresponding to the *default simulation*. On the one hand, the temperature anomalies in the *smaller box* simulation are less pronounced than in the *default simulation*. The strongest temperature anomalies are again close to the lower boundary, which supports our claim that these strong anomalies are boundary effects. On the other hand, the velocities of the *smaller box* simulation have lower values than those of the *default simulation*. This can be seen in more detail in Figure 4.12, where it is evident that the z-velocity average, the rms z-velocities and the average z-momentum are smaller than for those of the "default simulation". We suspect that both the temperature anomalies and the z-velocities are smaller because the box height is not large enough for the typical convective structures to develop undisturbed by boundary effects. Considering that the FLASH 1D-averaged vertical profiles agree very well with the PHOENIX/1D models, we can take this discrepancy in the 2D slices as a warning: different convective velocities and structures can result in correct 1D average profiles. Therefore, it is important to use a combination of analysis tools to determine the validity of the simulations.

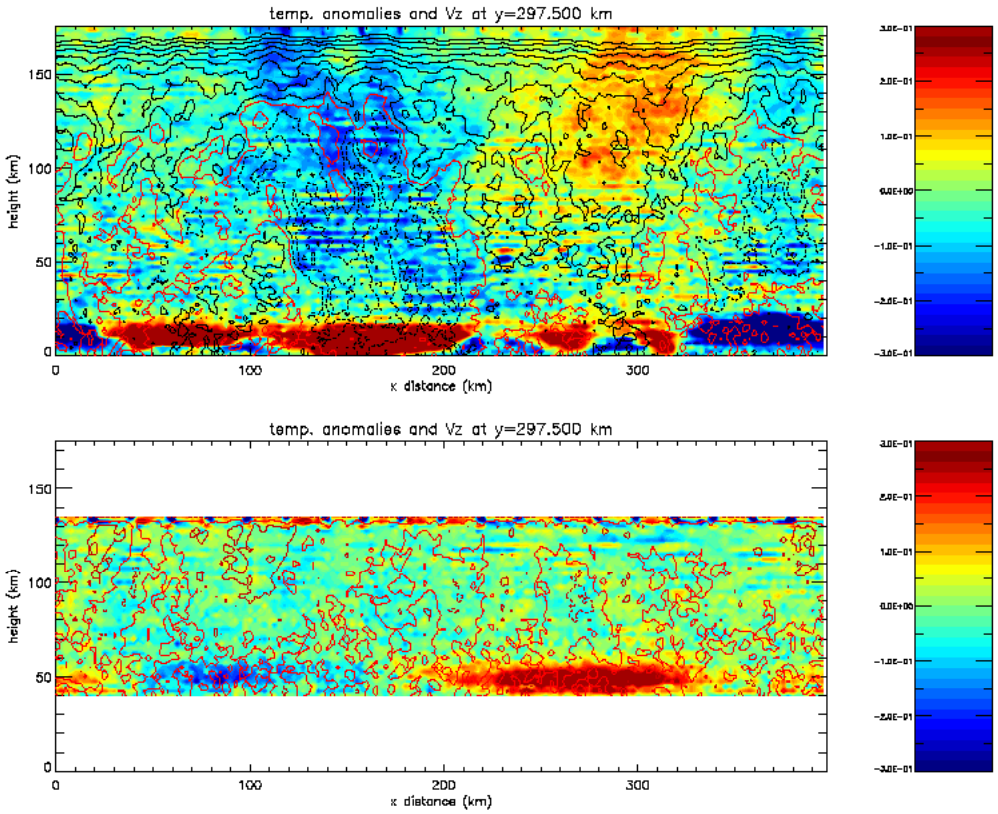

Figure 4.11: 2D vertical slices of the temperature anomalies for the *default simulation* (upper panel) and the for the simulation with a 100km high domain (lower panel). These anomalies are given as a percentage of the horizontal average value. The isocontours of the z-velocity field are plotted overlapping the temperature anomalies, with the isocontour of the zero z-velocity plotted in red, the negative z-velocities plotted in black dashed lines and the positive z-velocities plotted in continuous black lines.

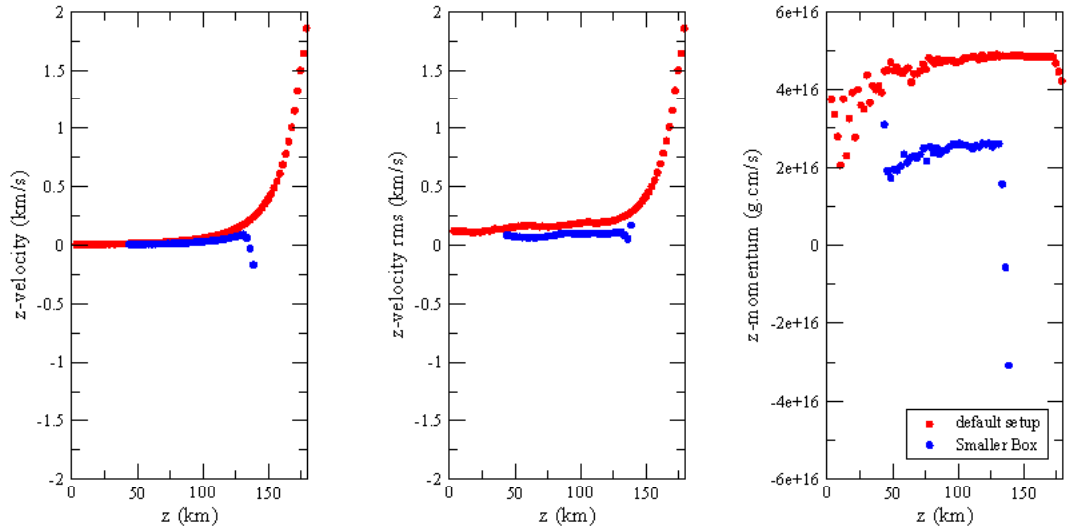

Figure 4.12: Horizontal averages of the z-velocity (left panel), rms z-velocity (middle panel) and horizontal average of the z-component of the momentum (right panel) as a function of altitude for the *default simulation* (red dots), and a a 100km high simulation (blue dots).

4.2.2 Lower boundary internal energy

The lower boundary of the simulation domain is within the convective region and allows inflows and outflows of material. The values of the density and the internal energy are fixed at the boundary using PHOENIX/1D models. We perform four simulations with 5% and 15% lower, and 5% and 15% higher values of the internal energy in the lower boundary (compared to those of the *default simulation*) to test how sensitive the simulations are to those changes. In Figure 4.13 we see that the FLASH 1D-averaged temperature profiles are shifted to higher temperatures for higher values of the internal energy in the lower boundary and to lower temperatures for smaller values of the internal energy. Higher densities and pressures are also observed for a higher internal energy in the lower boundary and viceversa. We conclude that the 1D average profiles are fairly sensitive to changes in the value of the internal energy in the lower boundary. It is also important to note here, that the temperature profiles are shifted, but the temperature gradient remains unchanged.

In Section 4.1.3, we found that the temperature profile for the *default simulation* is slightly shifted to higher temperatures with respect to the PHOENIX/1D model (Figure 4.6). Additionally, Figure 4.13 shows that a 5% decrease in the lower-boundary internal energy value results in a temperature profile that is now shifted to lower values with respect to the PHOENIX/1D model. From this result, we expect that a less pronounced decrease ($< 5\%$) of the internal energy at the lower boundary should be sufficient to correct for the temperature shift observed in the *default simulation*.

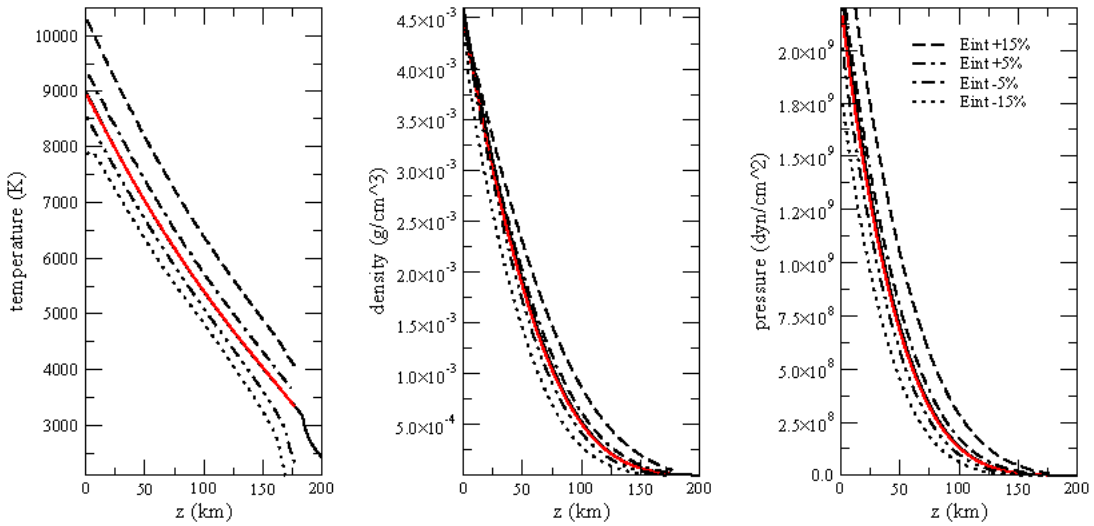

Figure 4.13: FLASH 1D-averaged vertical temperature, density and pressure profiles corresponding to a 5% bigger, 15% bigger, 5% smaller and 15% smaller lower-boundary-energy-values (various dot-dashed lines). The *default simulation* FLASH 1D-averaged vertical profiles (red line) and the PHOENIX/1D models (black line) are plotted as a reference.

Besides the changes in the temperature, density and pressure profiles, the different energy values in the lower boundary have a strong influence in the vertical velocity of the fluid. In the middle panel of Figure 4.14 we see that both increasing or decreasing the internal energy value in the lower boundary results in a significant increase in the rms z-velocities, particularly in the problematic upper part of the domain, compared to those of the *default simulation*. The average z-velocities (left panel Figure 4.14) and the z-momentum averages (right panel Figure 4.14) show that an increase in the lower boundary internal energy causes a net up-flow, worsening the problems that were observed for the *default simulation*. On the other hand, a decrease of more than 5% of the lower boundary internal energy values results in a net down-flow. We can conclude that all the four simulations with 5% and 15% lower, and 5% and 15% higher values of the internal energy in the lower boundary produce non equilibrium situations. Nevertheless, if we consider that the *default simulation* presents a shift to higher values in the temperature profile and a net downward flow, the effects of decreasing the internal energy value in the lower boundary, should modify the results in the right direction.

4.3 Tuning the lower boundary internal energy.

Based on the conclusions from the above section we can estimate that a decrease of around 2% in the lower-boundary internal energy value should be enough to correct the problems encountered in the "default simulation" (described in Sections4.1.1 and 4.1.3). Therefore, we

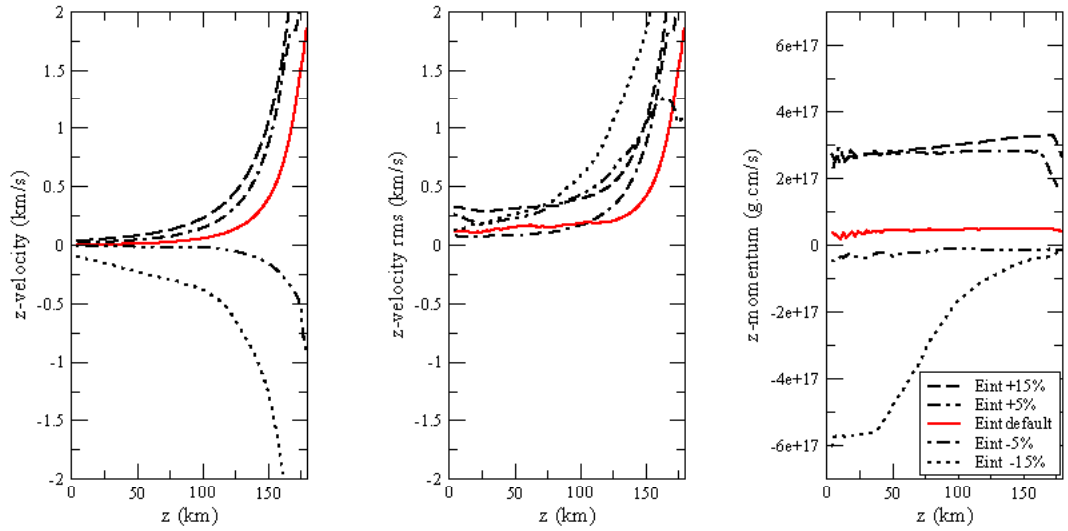

Figure 4.14: Horizontal averages of the z-velocity (left panel), rms z-velocity (middle panel) and horizontal average of the z-component of the momentum (right panel) as a function of altitude for simulations with 5% and 15% lower, and 5% and 15% higher values of the internal energy (various dot-dashed lines). The *default simulation* average z-velocity, rms velocity and average z-momentum are plotted in red as a reference.

perform a test simulation using the setup of the *default simulation* but with a 2% smaller value of the energy in the lower boundary. In the following, we will refer to this simulation as the *smaller energy simulation*

A zoom of the central region of the simulation domain (Figure 4.15) shows that the FLASH temperature profile for the *smaller energy simulation* very well with the PHOENIX/1D model, with a significant improvement with respect to the *default simulation*. The corresponding density and pressure profiles also agree better with the PHOENIX/1D model than those of the *default simulation*.

In addition to that, the 2% smaller lower-boundary internal energy clearly improves the z-velocity values. In the left panel of Figure 4.16 we can see that the z-velocity horizontal averages are all close to zero. The steep increase observed in the upper part of the domain of the *default simulation* is no longer present. The rms z-velocities (middle panel Figure 4.16) also improve: there is no increase in the upper region and, throughout the domain the resulting rms z-velocity values (of around 0.2km/s) are in very good agreement with those obtained by Wende et al. (2009) and by Freytag et al. (2010). Finally, the horizontal average z-momentum is zero or close to zero for every altitude (right panel Figure 4.16), indicating that there isn't a significant net mass flux and that the system is in equilibrium.

From the analysis of the 1D-averaged profiles and the z-velocity and momentum averages, we can conclude that a 2% decrease in the lower-boundary internal energy value, mends the

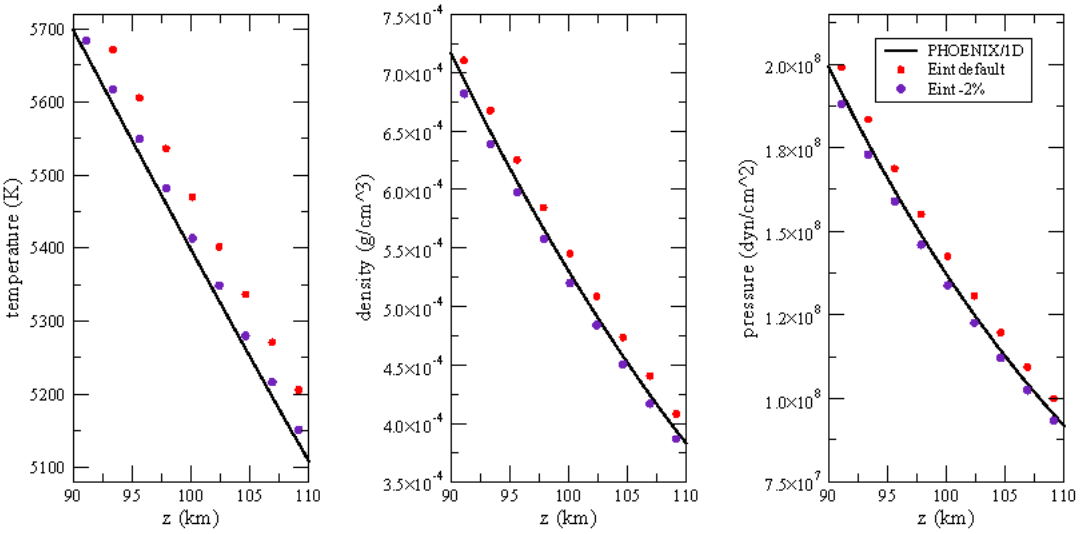

Figure 4.15: Zoomed-in view of the temperature, density and pressure profiles for the 1D-averaged FLASH results corresponding to a simulation with a 2% smaller internal energy value in the lower boundary (indigo dots). The *default simulation* FLASH 1D-averaged vertical profiles (red line) and the PHOENIX/1D models (black line) are plotted as a reference.

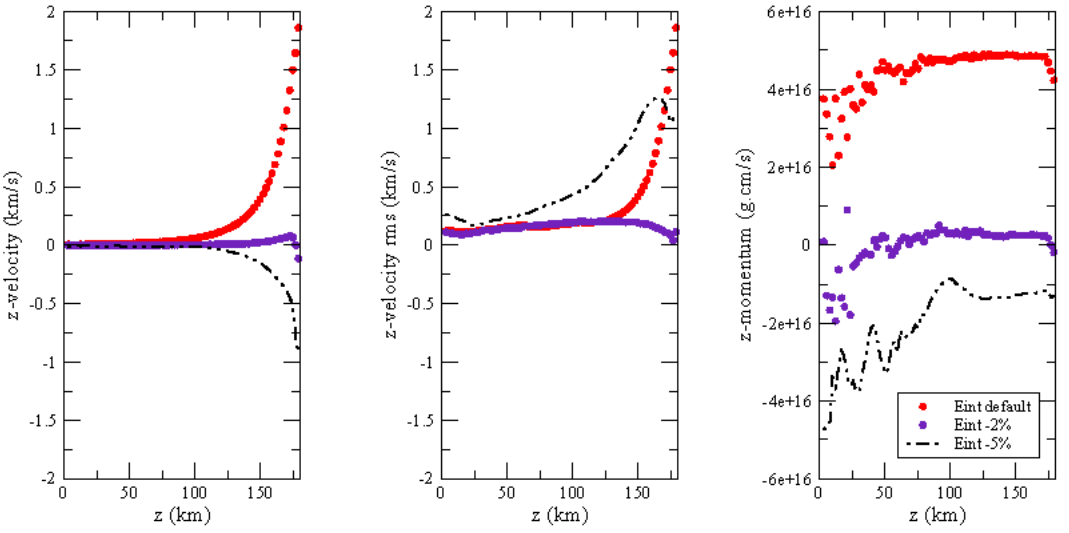

Figure 4.16: Horizontal average of the z-velocity (left panel), rms z-velocity (middle panel) and horizontal average of the z-component of the momentum (right panel) as a function of altitude for a simulation with 2% smaller lower-boundary-energy-value (indigo dots). The *default simulation* (red dots) and the 5% smaller lower-boundary-energy-value (dot-dashed line) average z-velocity, rms velocity and average z-momentum are plotted as a reference.

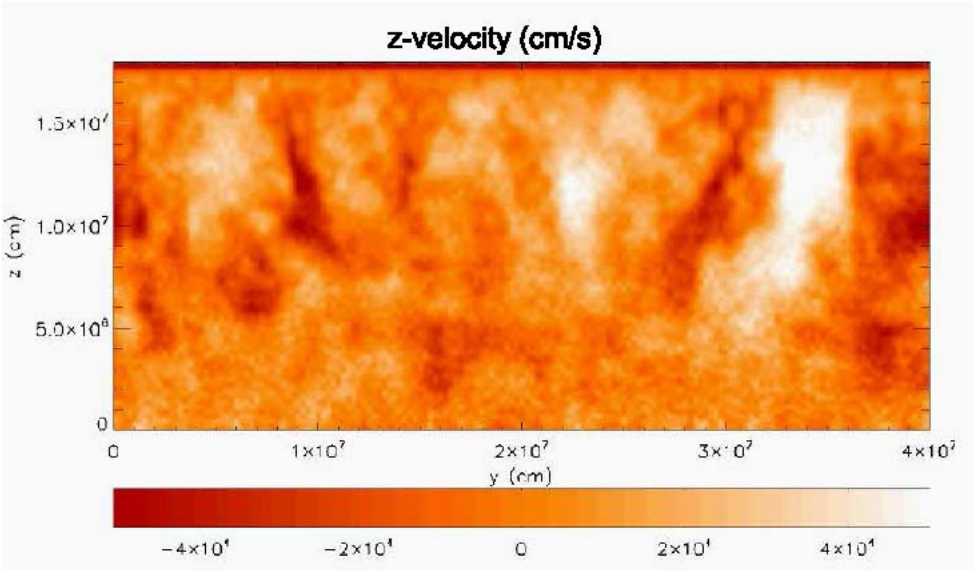

Figure 4.17: Vertical 2D slice of the z-velocity for a simulation with a 2% smaller value of the internal energy in the lower boundary. the brighter regions correspond to up-flows of material and the darker filaments correspond to down-flows.

problems encountered in the *default simulation*. Therefore, it is relevant to repeat in detail all the data analysis described in Sections 4.1.1 and 4.1.2, and see if the z-velocity structure and its correlation with temperature, density and pressure anomalies improve in this new simulation.

The first improvement can be seen in a 2D vertical slice of the velocity structure, where up-flows and down-flows of material consistent with convection are present throughout the whole domain (Figure 4.17), even in the upper part of the simulation, which was not the case for the *default simulation*. A second improvement is observable in the horizontal slices of the z-velocities for three different altitudes (Figure 4.18), where the granule-like structure is clearer and the contrast between up-flows and down-flows is stronger.

The 2D vertical slices of the temperature, density and pressure anomalies show again that the warmer regions are on average less dense and are going upwards and that the colder regions are on average denser and going downwards (Figure 4.19). These results are supported by the linear regressions of the temperature and density anomalies against the vertical velocity (Figure 4.20). In particular at $z = 100$ km we see that, for the *smaller energy simulation*, there is a stronger correlation between the warmer-less dense regions and the up-flows and the colder-denser regions and the down-flows, compared to the *default simulation*. We also note that at $z = 130$ km (right column Figure 4.20) the linear regression of the data is shifted compared to that of the *default simulation*. This is due to the fact that in the *smaller energy simulation* the average z-velocity is close to zero throughout the domain.

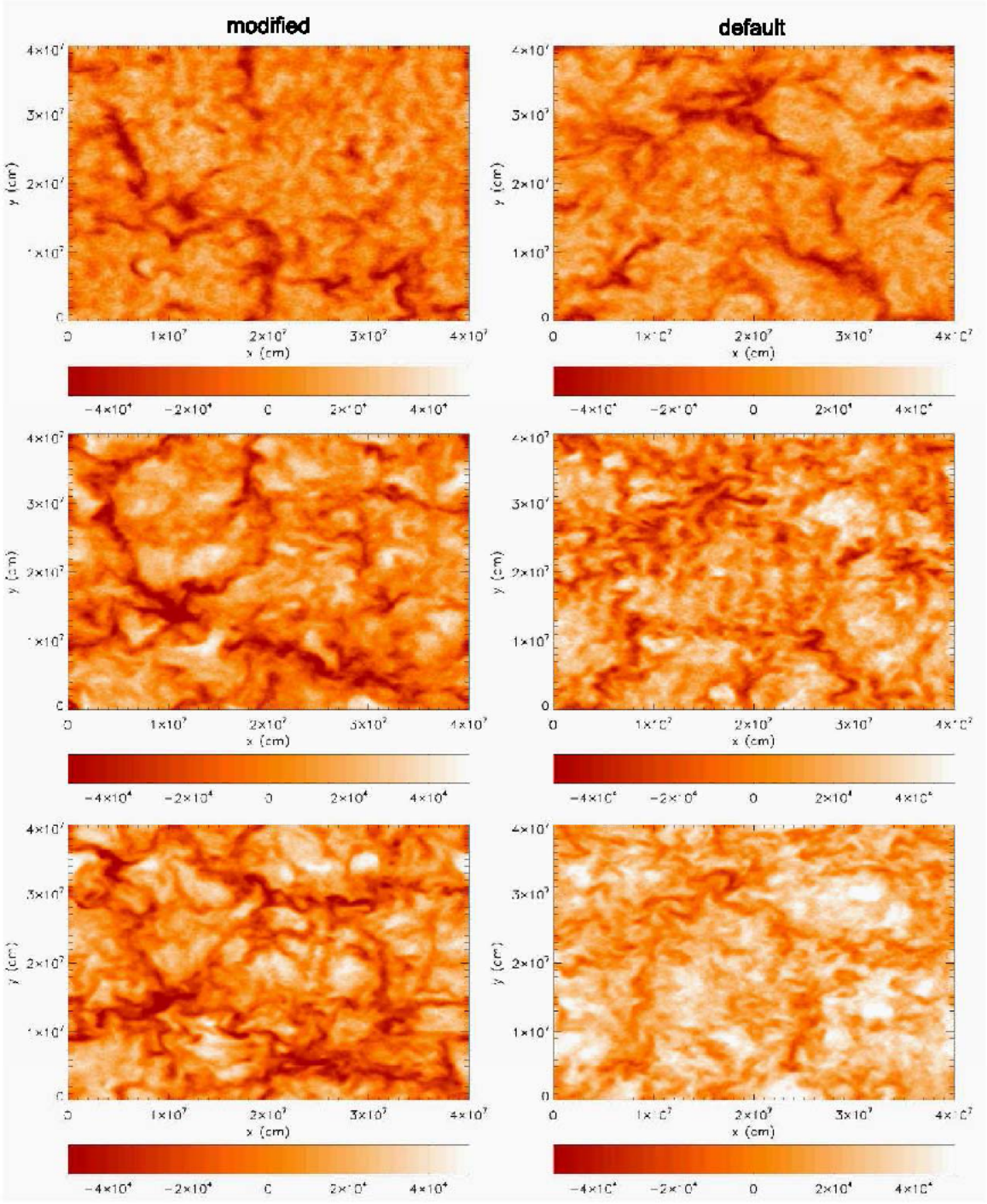

Figure 4.18: Horizontal slices of the z-velocity structure at three different heights: $z = 50$km (upper panels), $z = 100$km (middle panels) and $z = 130$km (lower panels). The left column corresponds to the 2% smaller lower-boundary-energy-value simulation and the right column corresponds to the *default simulation*. The brighter regions correspond to up-flows of material and the darker filaments correspond to down-flows.

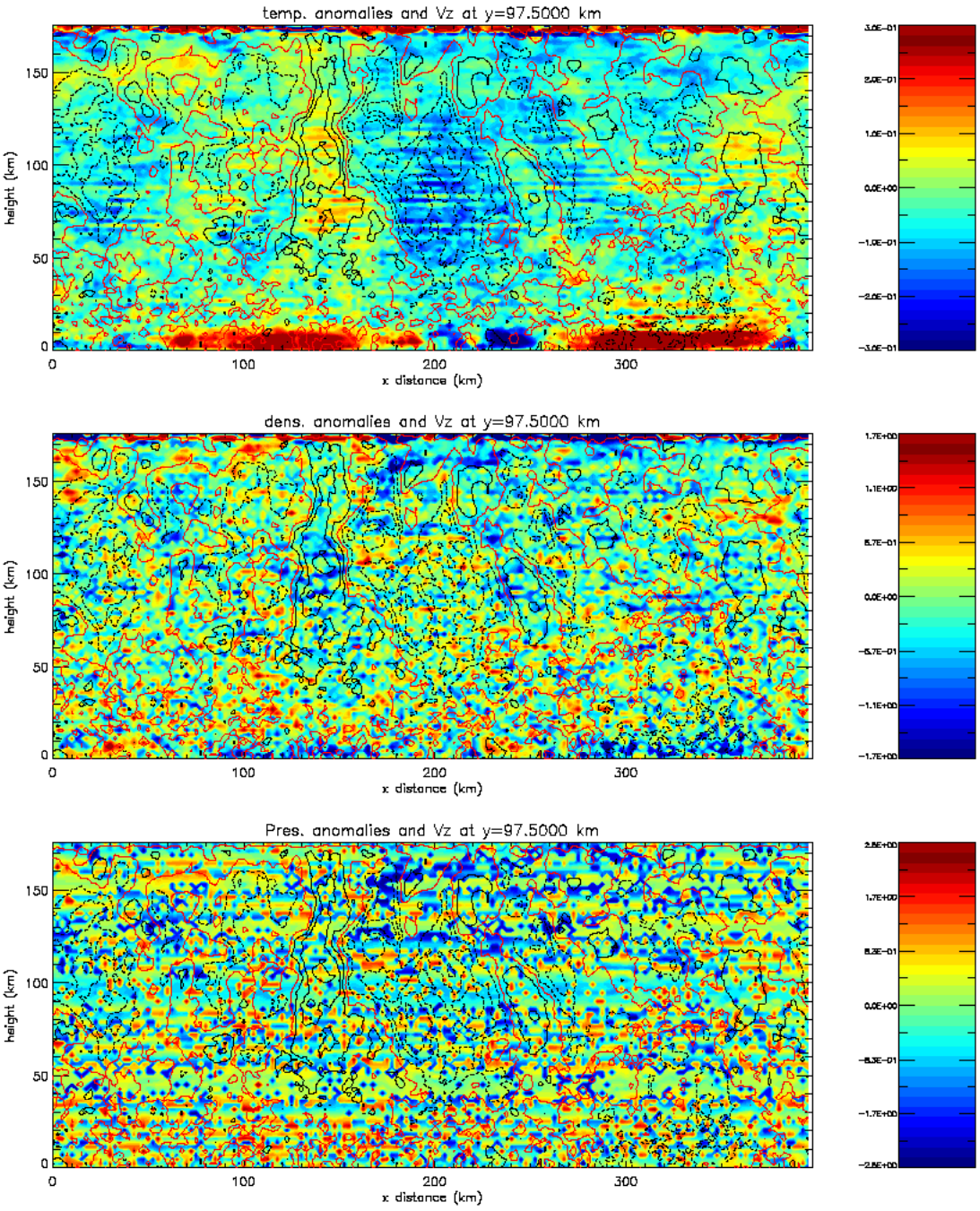

Figure 4.19: 2D vertical slices of the temperature (upper panel), density (middle panel) and pressure anomalies (lower panel), for the 2% smaller lower-boundary-energy-value simulation. These anomalies are given as a percentage of the horizontal average value. The isocontours of the z-velocity field are plotted overlapping the temperature, density and pressure anomalies, with the isocontour of the zero z-velocity plotted in red, the negative z-velocities plotted in black dashed lines and the positive z-velocities plotted in continuous black lines.

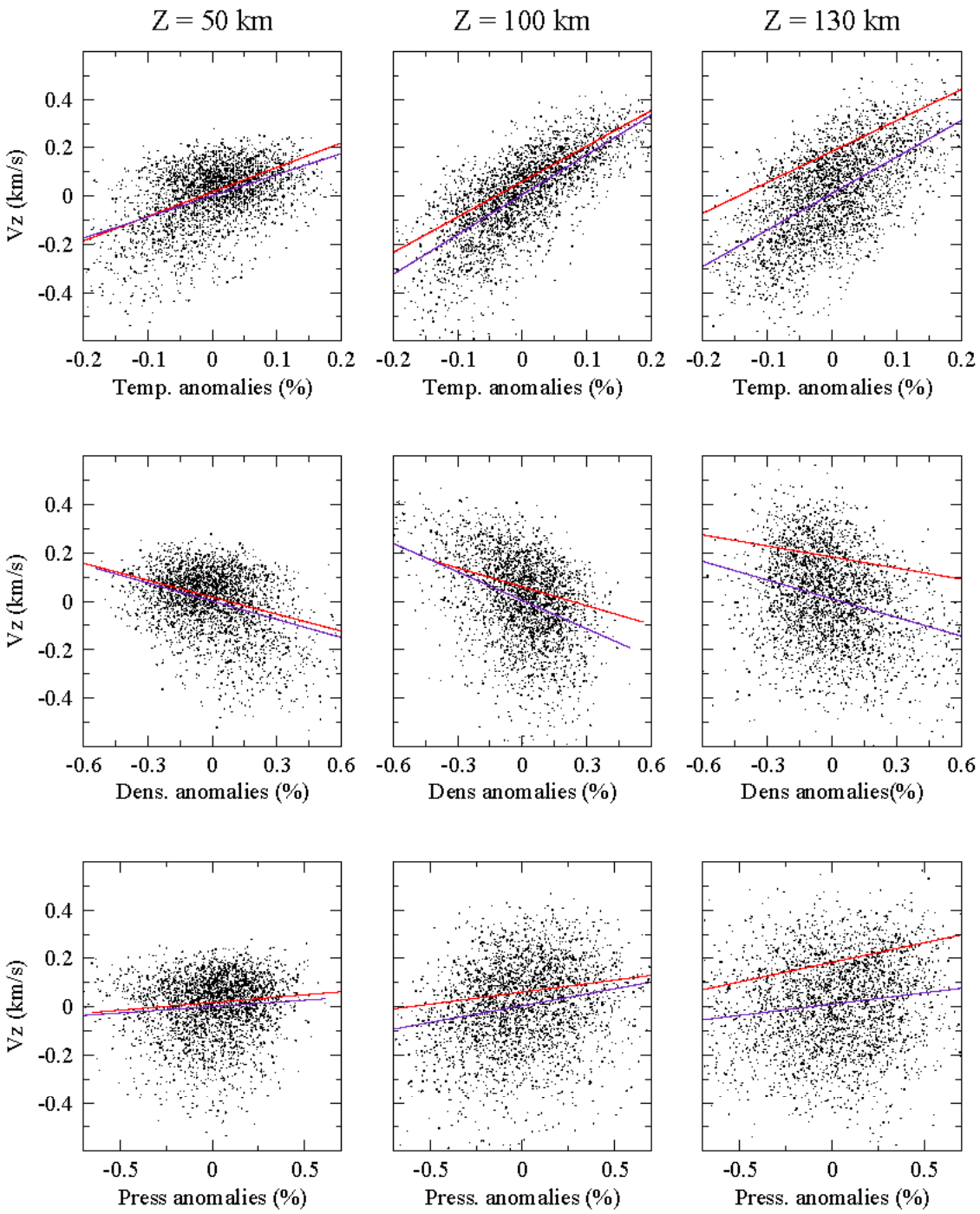

Figure 4.20: Scatter plots of temperature (upper row), density (middle row) and pressure (lower row) anomalies, against the vertical velocity at $z = 50$km (left column), $z = 100$km (middle column) and $z = 130$km (right column) for the 2% smaller lower-boundary-energy-value simulation. Each point corresponds to an average of $3 \times 3 \times 3$ gird cells. The indigo line corresponds to a linear regression of the data. The red line corresponds to the linear regression obtained for the *default simulation* data and is plotted as a reference.

	slope	intercept	correlation coefficient
temp 50km	0.876	0.001	0.469
dens 50km	-0.251	0.001	-0.359
pres 50km	0.052	0.000	0.086
temp 100km	1.649	0.005	0.738
dens 100km	-0.393	0.004	-0.382
pres 100km	0.139	0.004	0.204
temp 130km	0.738	0.010	0.612
dens 130km	-0.257	0.011	-0.300
pres 130km	0.093	0.011	0.153

Table 4.2: Correlation coefficients and linear regression parameters corresponding to the scatter plots of the 2% smaller lower-boundary-energy-value simulation in Figure 4.20.

4.4 Impact of the upper boundary internal energy.

In Section 4.2.2 we showed how the lower-boundary-value of the internal energy plays a crucial role in the resulting temperature, density and pressure averaged profiles, as well as in the z-velocity structures. Furthermore, in Section 4.3, we found that even a tiny 2% decrease in the lower-boundary internal energy, resulted in significant changes, in particular in the z-velocities of the system. Since in the simulation setup process we also use the PHOENIX/1D models to determine the internal energy value in the upper boundary, it is relevant to study how sensitive are the results to changes in these upper-boundary internal energy values. We perform two test simulations, one with a 10% increase and one with a 10% decrease in the upper-boundary internal energy values. We use as a reference the *smaller energy simulation*.

In Figure 4.21 we see that there is a very good general agreement between the FLASH temperature, density and pressure structures with a modified upper-boundary internal energy and the PHOENIX/1D models. This good agreement indicates that the upper-boundary internal energy value has not a significant influence in the resulting temperature, density and pressure structures. This is further confirmed by zooming in, both in a middle (Figure 4.22) and in an upper (Figure 4.23) region of the simulation domain. There are some small shifts in the profiles but those are negligible compared to those produced by changes in the lower-boundary-energy-value. This result is very important, because it means that the resulting FLASH-1D averaged temperature, density and pressure structures are not determined by the upper-boundary-energy-value. It is therefore meaningful to use the PHOENIX/1D models as a tool to test the FLASH simulations.

Besides the temperature, density and pressure profiles, it is relevant to study the effect of the

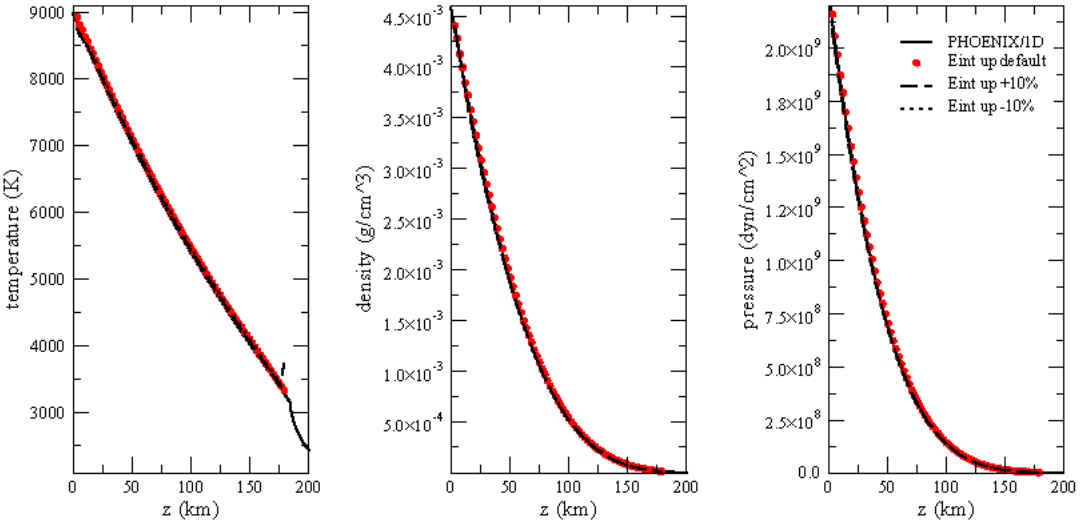

Figure 4.21: FLASH 1D-averaged vertical temperature, density and pressure profiles corresponding to a 10% bigger (dashed line) and 10% smaller (dotted line) upper-boundary-energy-values. The *default simulation* FLASH 1D-averaged vertical profiles (red dots) and the PHOENIX/1D models (black line) are plotted as a reference.

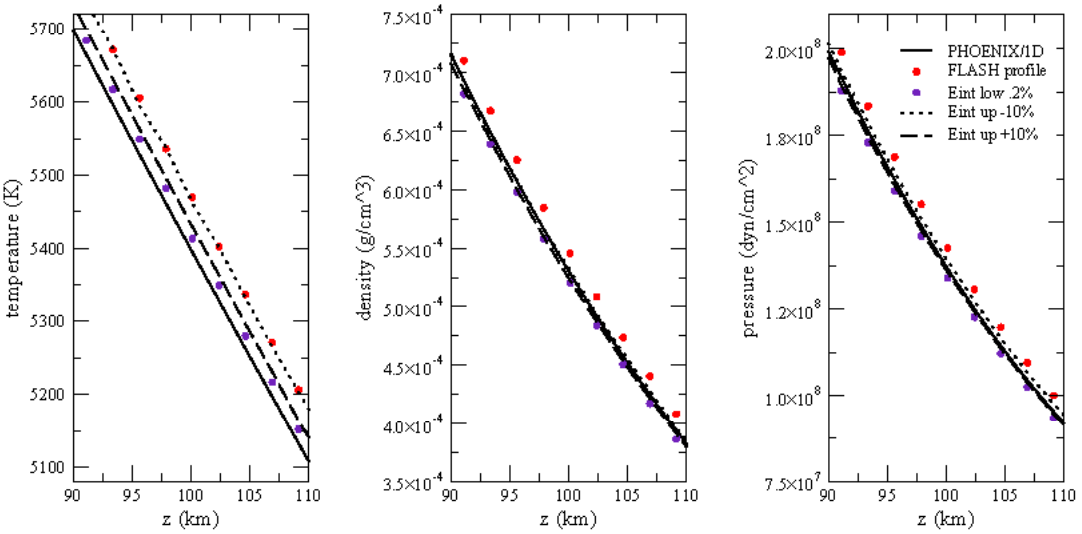

Figure 4.22: Middle region zoomed-in view of the temperature, density and pressure profiles for the 1D-averaged FLASH results corresponding to a simulation with a 10% bigger (dashed line) and 10% smaller (dotted line) upper-boundary-energy-values. The *default simulation* FLASH 1D-averaged vertical profiles (red dots), the *smaller energy simulation* (indigo dots) and the PHOENIX/1D models (black line) are plotted as a reference.

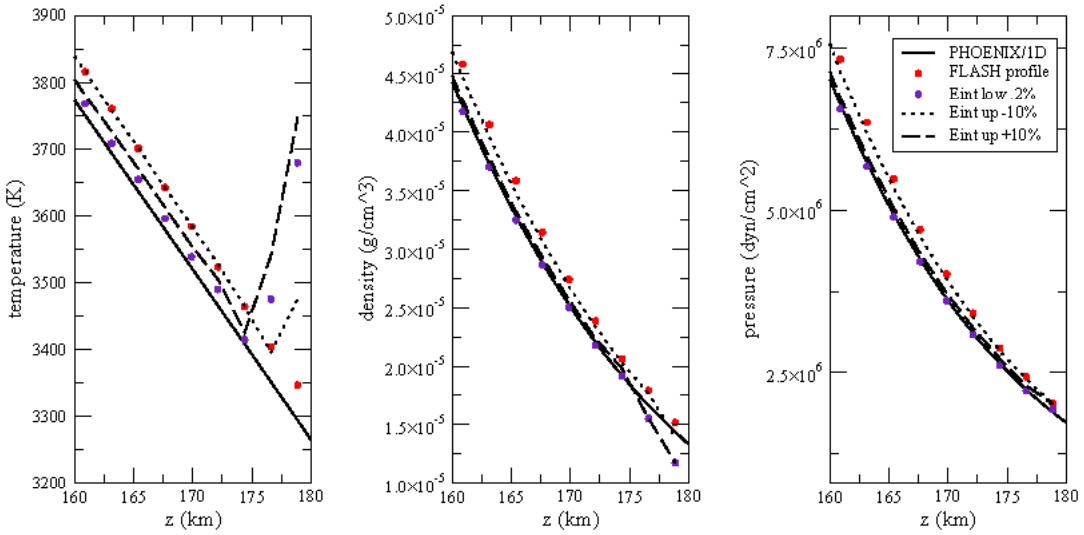

Figure 4.23: Upper region zoomed-in view of the temperature, density and pressure profiles for the 1D-averaged FLASH results corresponding to a simulation with a 10% bigger (dashed line) and 10% smaller (dotted line) upper-boundary-energy-values. The *default simulation* FLASH 1D-averaged vertical profiles (red dots), the *smaller energy simulation* (indigo dots) and the PHOENIX/1D models (black line) are plotted as a reference.

upper-boundary-energy-value in the vertical velocity of the fluid. We can see in Figure 4.24, that both a 10% increase or decrease in the upper-boundary-energy-value have little effect in the averaged z-velocities, the rms z-velocities or in the z-momentum averages. This analysis reinforces the evidence that changes in the upper-boundary-energy-value have a negligible impact in the simulations.

4.5 Discussion: stability of the simulations

In all the previous Sections we have considered and analyzed snapshots of the system. We use the temporal evolution of integral quantities, such as the total z-momentum or the total mass of the system, to determine when the simulation has reached a stationary state. In Figures 4.26 and 4.25 we can distinguish three different stages. For $t < 1750$s there are strong oscillations of both the total mass and total z-momentum. These oscillations decrease with time as the system evolves to a state of equilibrium. From $t = 1750$s to $t = 2500$s the mass has a constant value and the z-momentum has very small oscillations around zero, which indicates that there is not net flux of mass through the boundaries. During this time interval we can consider that the system is in a stationary state, and it is for time steps in this interval that we take the snapshots used in the analysis. Once the system reaches a quasi-stable state, it should remain in it.

Nevertheless, starting at $t \approx 2500$s there is an unexpected increase in the total momentum

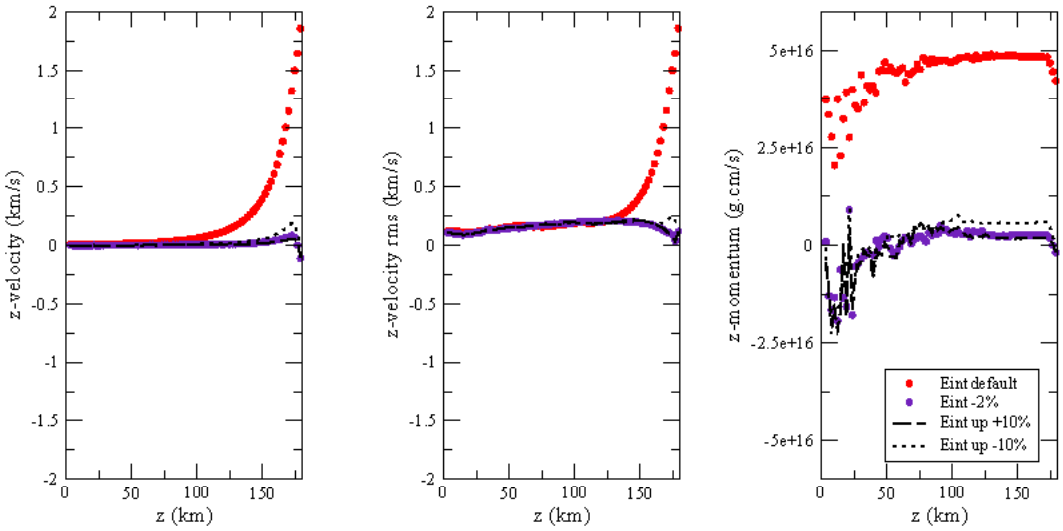

Figure 4.24: Horizontal averages of the z-velocity (left panel), rms z-velocity (middle panel) and horizontal average of the z-component of the momentum (right panel) as a function of altitude for simulations with a 10% bigger (dashed line) and 10% smaller (dotted line) upper-boundary-energy-values. The average z-velocity, rms velocity and average z-momentum correspondign to the *smaller energy simulation* are plotted in indigo dots as a reference.

of the system while the total mass remains constant (see Figures 4.26 and 4.25). There is no apparent reason to explain this sudden increase in the total z-momentum of the system, and therefore, we suspect that some numerical instability is responsible for this behavior. This hypothesis reinforced by the plots of the evolution of the total x and y-momentum (See Figure 4.27). Since we have periodic boundary conditions and no forcing in the x and y direction (as described in section 3.2), we expect the x and y-momentum to be close to zero for symmetry reasons. However, in Figure 4.27, it is evident that the total x and y-momentum are not zero, and at $t \approx 2500$ their absolute values start to increase, with the total x-momentum having negative values and the total y-momentum having positive values. There is clearly no physical explanation, and therefore we believe that the system becomes unstable due to numerical problems.

We described in Section 2.2 that the PPM hydrodynamical method uses an operator splitting technique (Strang, 1968), so that the 3D equations are solved as a succession of 1D problems. We believe that this splitting method could be responsible for introducing the non-physical asymmetries observed for the total x and y-momentum (See Figure 4.27). A new "unsplit" solver has been recently included in the FLASH code distribution and could be tested in a future set of simulations, but this is beyond the scope of this work.

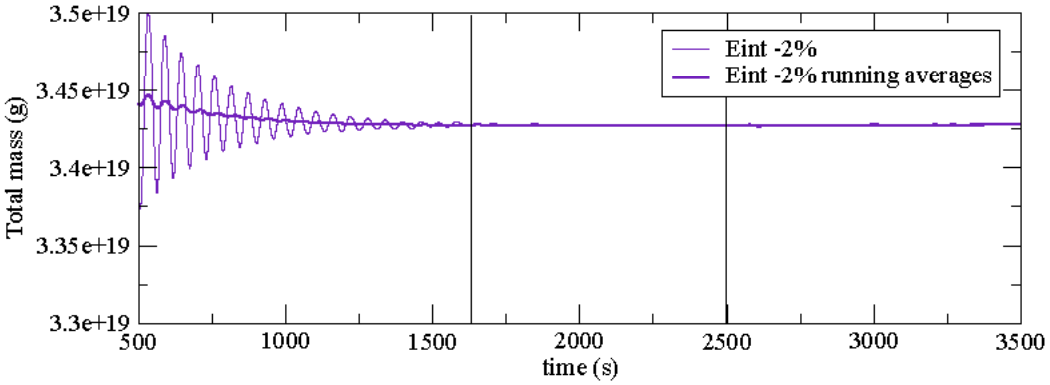

Figure 4.25: Time evolution of the total mass of the system (indigo thin line). 1000 data points running averages (around 100s) are also plotted (thick line).

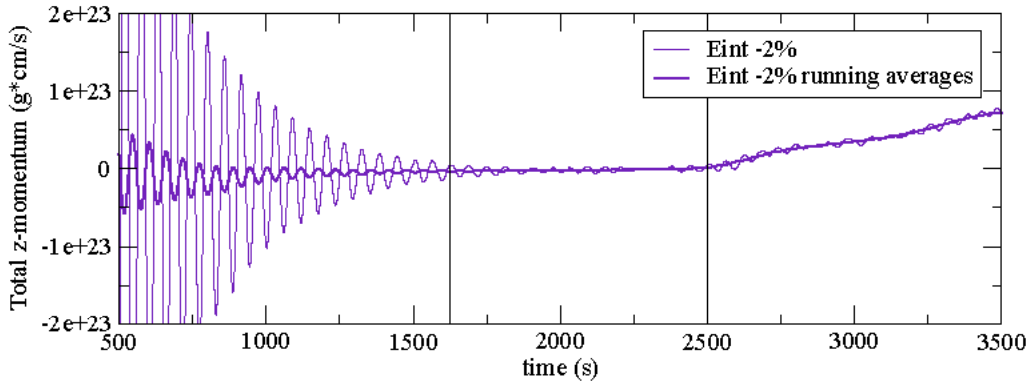

Figure 4.26: Time evolution of the total z-momentum of the system (indigo thin line). 500 data points running averages (around 50s) are also plotted (thick line).

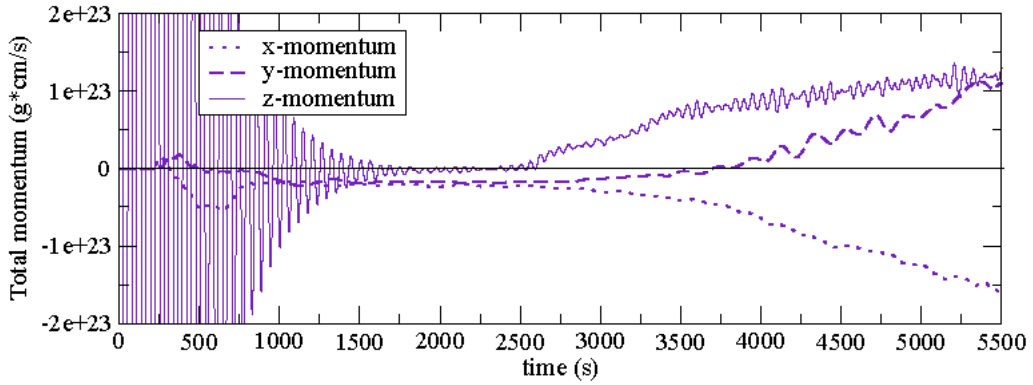

Figure 4.27: Time evolution of the total x-momentum (dotted line), y-momenutm (dashed line) and z-momentum (solid line) of the system.

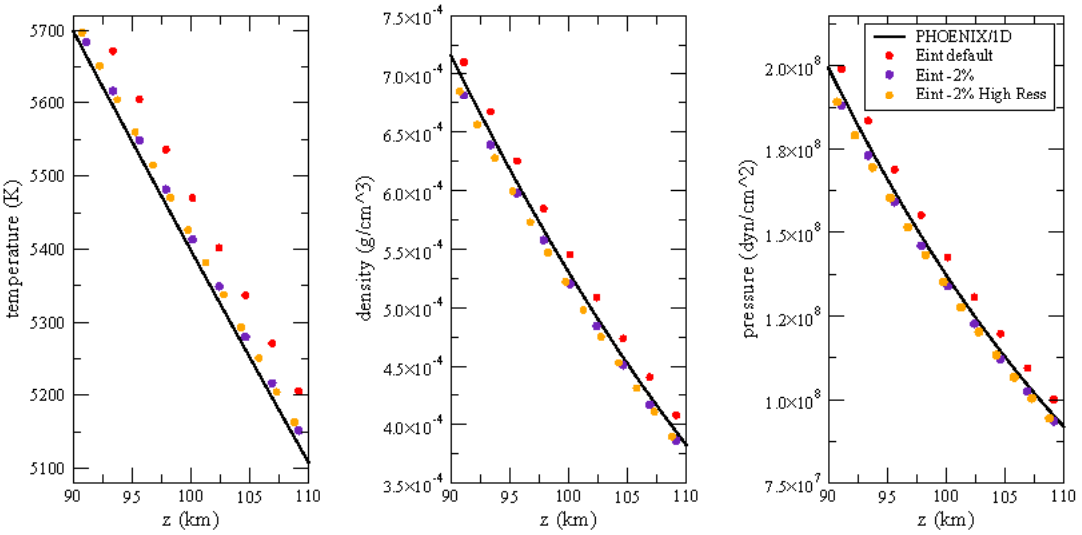

Figure 4.28: Zoomed-in view of the temperature, density and pressure profiles for the 1D-averaged FLASH results corresponding to the *smaller energy simulation* with *default resolution* (indigo dots) and with a *higher resolution* (orange dots). The *default simulation* FLASH 1D-averaged vertical profiles (red dots) and the PHOENIX/1D models (black line) are plotted as a reference.

4.6 A higher resolution simulation

We described in Section 3.1 that convection occurs in many different lenght scales and that in an ideal situation, one should resolve even the smallest turbulent structure. Nevertheless, due to computational limitations, it is necessary to restrict the resolution. For all the simulations presented above, the box size is 400 km $\times$400 km $\times$160 km, with a resolution of $160\times160\times80$, which corresponds to a grid-cell size of 2.5 km (we will call this the *default resolution*). This grid-cell size is presumeably larger than the smallest turbulent scales of the system. To test if the unresolved structures have an influence in our results, we repeat in this Section the *smaller energy simulation*, but with a higher resolution. For the same box size, we use $240\times240\times120$ grid cells resulting in a grid-cell size of 1.5 km (we will call this the *higher resolution*).

A zoom of the central region of the simulation domain (Figure 4.28) shows that the FLASH temperature, density and pressure profiles are the same for the two different resolutions. In addition to that, we can see no significant differences in the horizontal averaged z-velocities, the rms z-velocities and the horizontal averaged z-momentum for the two resolutions (Figure 4.29). These results indicate that this newly resolved smaller scale turbulence does not seem to have a significant effect on the mean temperature, density and pressure profiles, or in the averaged z-velocities and z-momentum.

An improvement with the *higher resolution* is evident in the horizontal slices of the z-velocities for three different altitudes (Figure 4.30), where more granule-like structures are

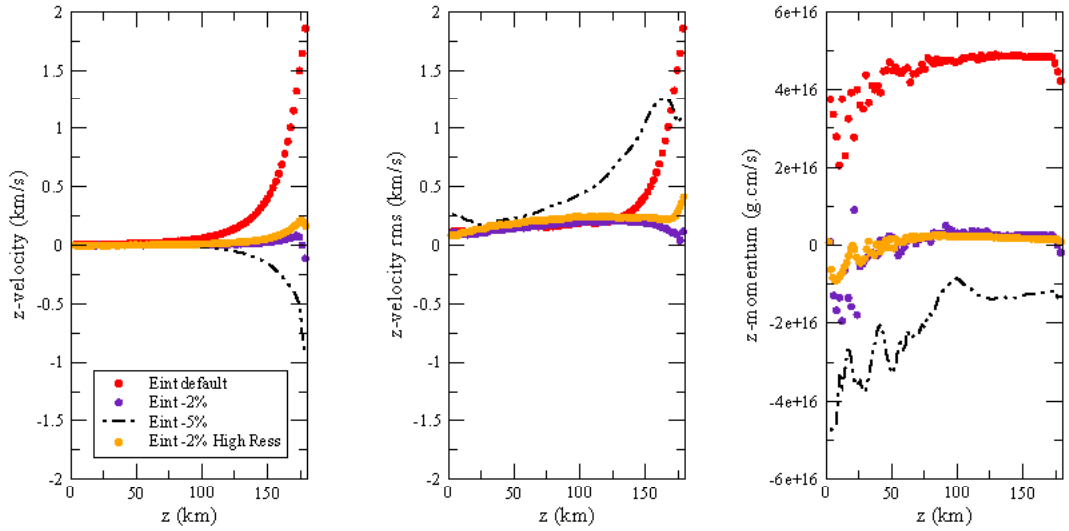

Figure 4.29: Horizontal average of the z-velocity (left panel), rms z-velocity (middle panel) and horizontal average of the z-component of the momentum (right panel) as a function of altitude for the *smaller energy simulation* with *default resolution* (indigo dots) and with a *higher resolution* (orange dots). The *default simulation* (red dots) and the 5% smaller lower-boundary-energy-value (dot-dashed line) average z-velocity, rms velocity and average z-momentum are plotted as a reference.

visible and the contrast between up-flows and down-flows is stronger than for the *default resolution*. A more detailed structure can also be seen in the 2D vertical slices of the temperature, density and pressure anomalies (Figure 4.31). In this figure we can see once again that the warmer regions are on average less dense and are going upwards, and that the colder regions are on average denser and going downwards. But the most significant improvement of the high resolution simulation is that the strong temperature anomalies attributed to boundary effects (see for example Figure 4.20) are no longer present. This leads to a significant increase in the correlations in the lower part of the domain (Figure 4.32 and Table 4.3).

We conclude that an increase in the resolution has little effect on the mean vertical temperature, density and pressure profiles of the simulation, as well as in the mean z-velocities, rms z-velocities and mean z-momentum. This is an indication that the small scale turbulence —or at least the newly resolved small scale turbulence in the *higher resolution simulation*— has a negligible effect in the overal convective dynamics, in accordance with results of the solar simulations by (Stein and Nordlund, 1998). The higher resolution has nevertheless a positive impact, since the boundary effects on the temperature anomalies are no longer present in the *higher resolution* simulation.

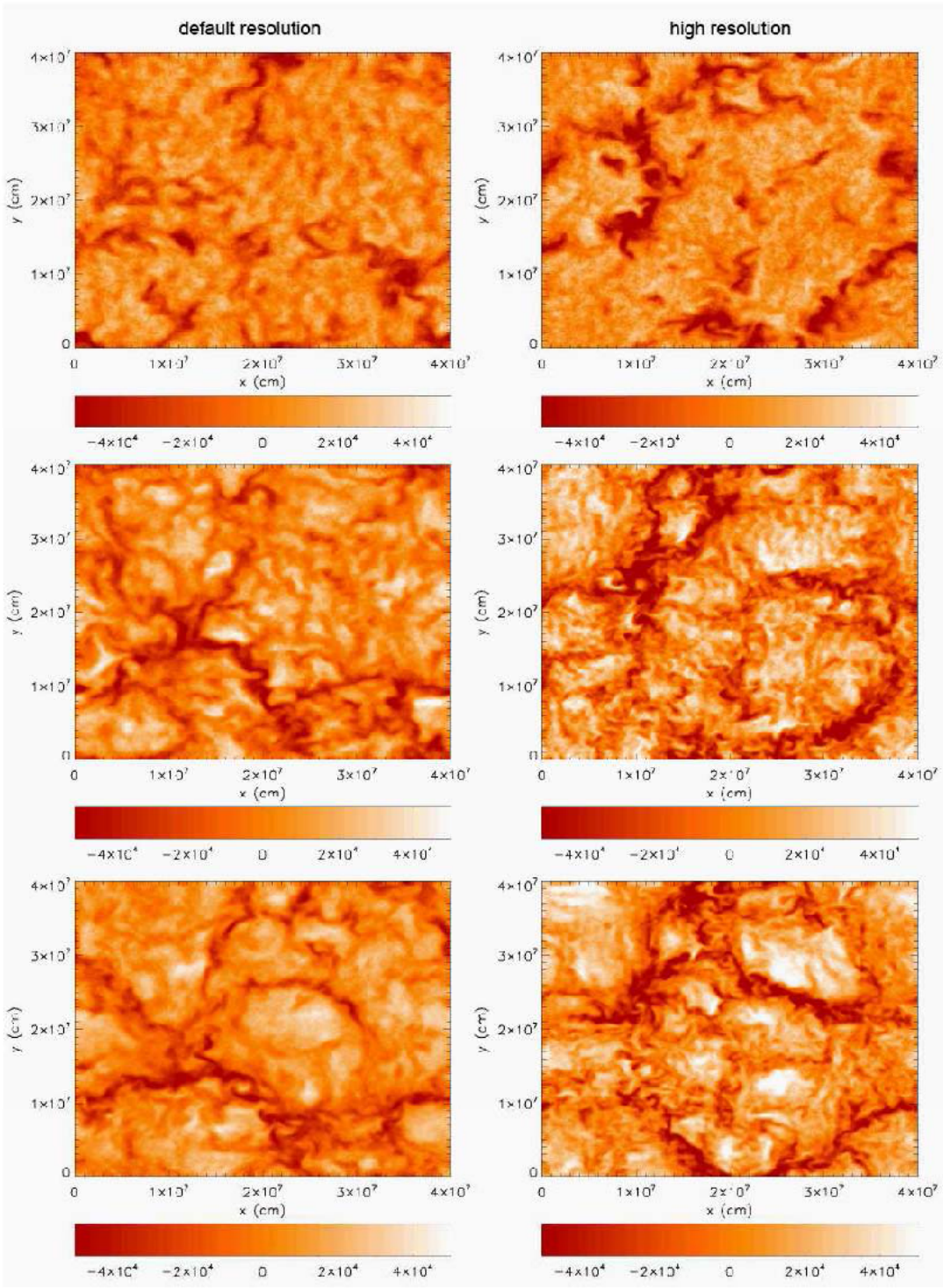

Figure 4.30: Horizontal slices of the z-velocity structure at three different heights: $z = 50$km (upper panels), $z = 100$km (middle panels) and $z = 130$km (lower panels) for a 2% smaller lower-boundary-energy-value simulation. The left column corresponds to the *default resolution simulation* and the right column corresponds to the *higher resolution simulation*. The brighter regions correspond to up-flows of material and the darker filaments correspond to down-flows.

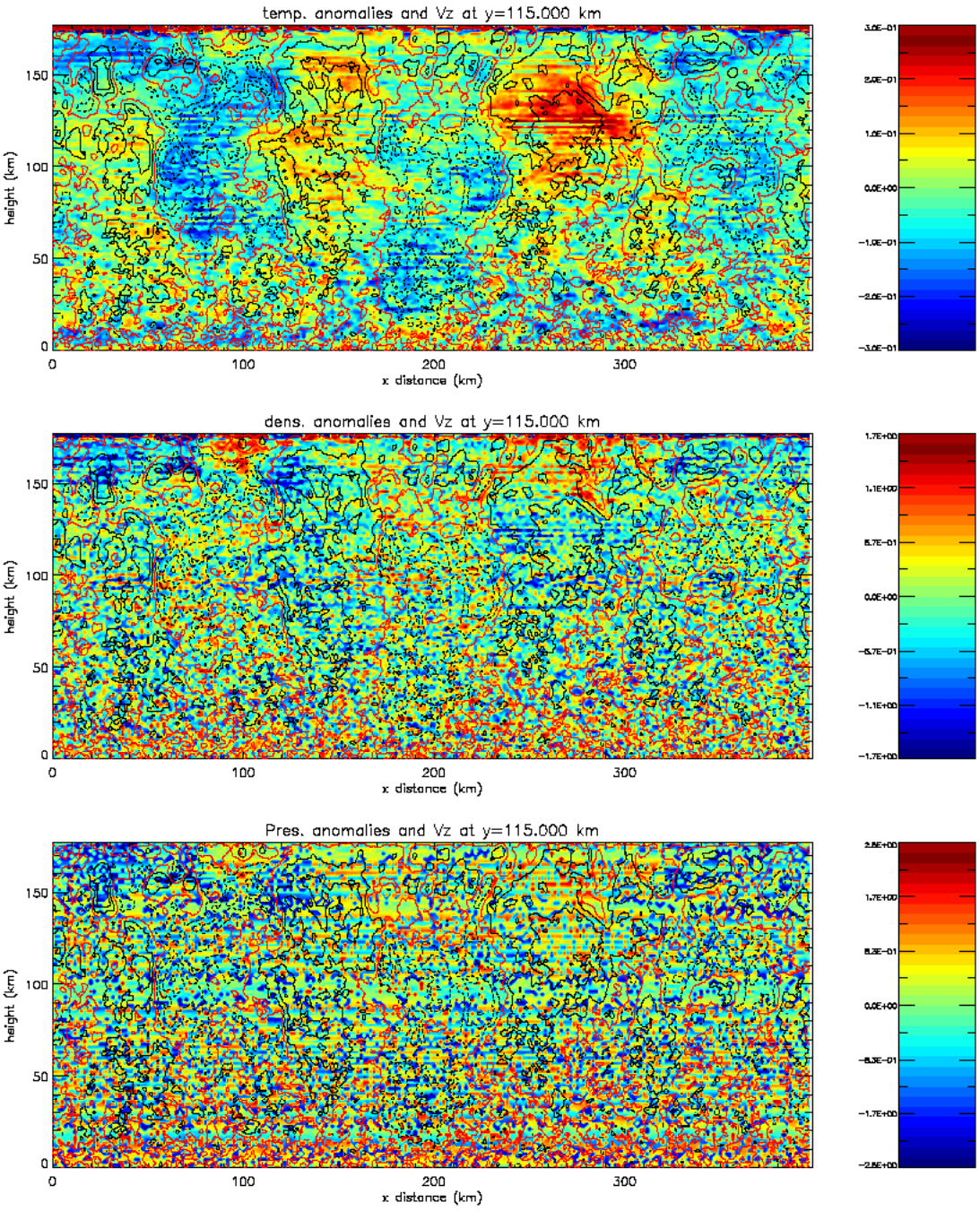

Figure 4.31: 2D vertical slices of the temperature (upper panel), density (middle panel) and pressure anomalies (lower panel), for the *higher resolution simulation*. These anomalies are given as a percentage of the horizontal average value. The isocontours of the z-velocity field are plotted overlapping the temperature, density and pressure anomalies, with the isocontour of the zero z-velocity plotted in red, the negative z-velocities plotted in black dashed lines and the positive z-velocities plotted in continuous black lines.

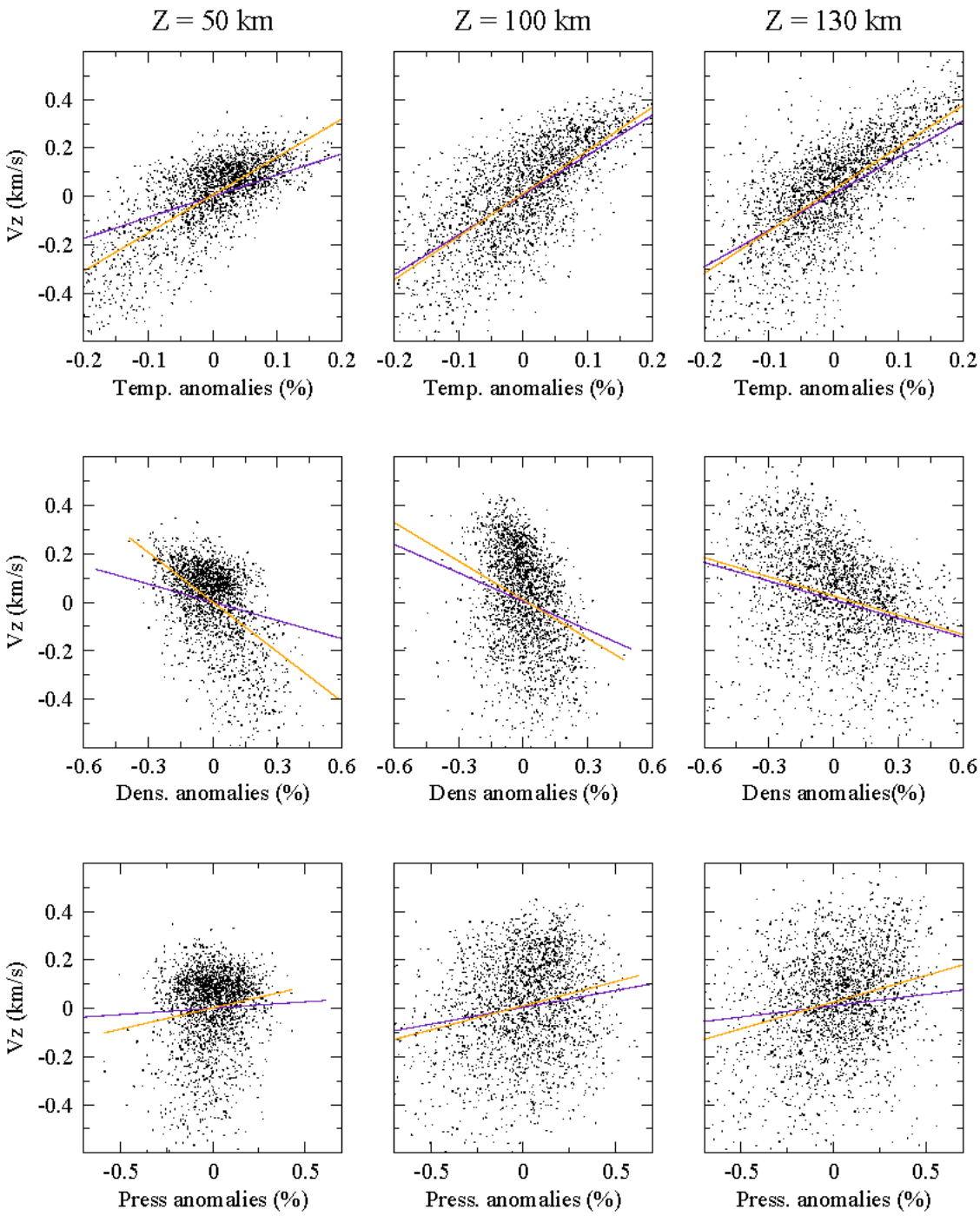

Figure 4.32: Scatter plots of temperature (upper row), density (middle row) and pressure (lower row) anomalies, against the vertical velocity at $z = 50$km (left column), $z = 100$km (middle column) and $z = 130$km (right column) for the *higher resolution simulation*. Each point corresponds to an average of $3 \times 3 \times 3$ gird cells. The orange line corresponds to a linear regression of the data. The indigo line corresponds to the linear regression obtained for the *default resolution* data and is plotted as a reference.

	slope	intercept	correlation coefficient
temp 50km	1.573	0.005	0.756
dens 50km	-0.686	0.001	-0.524
pres 50km	0.175	0.002	0.145
temp 100km	1.780	0.011	0.712
dens 100km	-0.533	0.011	-0.296
pres 100km	0.199	0.010	0.230
temp 130km	1.734	0.028	0.696
dens 130km	-0.264	0.026	-0.309
pres 130km	0.219	0.026	0.296

Table 4.3: Correlation coefficients and linear regression parameters corresponding to the scatter plots in Figure 4.32.

Chapter 5

Conclusions and outlook

Convection is the main energy transport mechanism in the interior of substellar objects and, therefore, plays a crucial role in their structure. As a first step towards the explicit simulation of convection in substellar objects, we coupled a state of the art equation of state (ACES-EOS) to the hydrodynamic FLASH code. This ACES-EOS includes chemical processes such as molecule formation, and can be used for simulations with temperatures as low as 100K. From the thermodynamical variables calculated by the ACES-EOS, we derived the adiabatic index Γ. This adiabatic index plays a crucial role in the numerical solution of the hydrodynamic equations and was successfully tested during the ACES-EOS coupling process: we found a good agreement between the Γ calculated from the ACES-EOS variables and values obtained by Dorfi (1998). This good agreement is also a validation of the ACES-EOS internal energy and entropy values, since those variables are explicitly required in the Γ calculation.

Having achieved this coupling, we focused on testing the "FLASH+ACES-EOS" code on a more realistic problem. In order to do so, we simulated convection locally, for an object with effective temperature $T_{\rm eff}$=2800 K and surface gravity $\log(g)$=5.0 (in cgs units). Our setup consisted of a 400 km $\times$400 km $\times$160 km box embedded in the upper part of the convective region of the object. We fixed the internal energy and density values at the upper and lower boundaries and used a PHOENIX/1D model atmosphere, both to determine those boundary values and to construct initial conditions. The sensitivity of our simulations to these boundary and initial conditions was tested. We found that the results are independent of the initial conditions and of changes in the upper-boundary internal energy, whereas they are strongly influenced by the lower-boundary internal energy. We also found that a 2% decrease in the lower-boundary energy value, with respect to the one provided by the PHOENIX/1D model, significantly improves the results of our hydrodynamic simulation.

To characterize and validate our results, we use both qualitative and quantitative methods. In a first qualitative analysis of the z-velocity horizontal slices of the domain, we found granule-like regions of material moving upwards, surrounded by filament-like structures of sinking material. This overall z-velocity structure is similar to the granular structure observed in the

Sun (Stein and Nordlund, 1998), and is also very similar to the "deeper-layer" slices of the M-dwarf simulations by Ludwig (2006). Additionally, the correlation analysis between vertical velocity and temperature, density and pressure anomalies, shows that warmer and less dense regions move upwards while colder denser regions move downwards, which is a clear indication of convection.

For a more quantitative validation of the results, we compared FLASH 1D-averaged vertical profiles with the PHOENIX/1D temperature, density and pressure profiles, and found a very good general agreement between the two models. This indicates, on the one hand, that the FLASH simulation is on average in hydrostatic equilibrium (or at least very close to hydrostatic equilibrium), and, on the other hand, that convective energy transport is correctly calculated in the FLASH model, since the temperature structure is determined by the energy transport in the system. As a final validation, we obtained rms z-velocities values of around 0.2km/s that are in very good agreement with those obtained by Wende et al. (2009) and by Freytag et al. (2010). Additionally, the horizontal average z-momentum is zero or close to zero for every altitude, indicating that there isn't a significant net mass flux and that the system is in equilibrium.

We encountered numerical boundary effects that arise as strong anomalies—unrelated to convective motions—in the temperature and density fields, very close to the lower boundary. However, these boundary effects disappear if we increase the resolution of the simulation, while the convective-related features of the lower resolution simulation are maintained. We found once again granule-like structures, with warmer and less dense regions moving upwards and colder denser regions moving downwards. The FLASH mean profiles agree very well with the PHOENIX/1D models and the rms z-velocity values are similar to those obtained by Wende et al. (2009) and by Freytag et al. (2010). All these results indicate that convection is correctly simulated by the FLASH code coupled to the ACES-EOS. With this validation process completed, it is possible in a future work to perform simulations for lower temperatures and lower masses.

The above described results correspond to a stationary state of the system that occurs for a finite time interval, which is long enough to cover several convective times scales (Freytag et al., 2010). However, if we want to include processes with longer time scales, such as dust formation, the long term stability of the system has to be revised. Our simulations indicate that a numerical problem can be the cause for a long term instability that arises after 2500 seconds. We suspect that the operator splitting technique (Strang, 1968) used by the PPM hydrodynamic solver in the FLASH code could be responsible for introducing non-physical asymmetries and suggest in the future to use the new "unsplit" solver that has been recently included in the FLASH code distribution.

Furthermore, note that our simulations were limited to the purely convective layer, since the FLASH code does not include radiative processes yet. However, very interesting hydrody-

namic phenomena, such as convective overshooting or gravity waves, occur in the transition region between the convective and the radiative layers. Therefore, a crucial next step would be to include radiative processes in our simulation by adding a radiative transfer solver into the FLASH code. This would enable us to simulate higher levels in the atmosphere and the resulting temperature, density, pressure and velocity structures could be used as input structures in the PHOENIX/3D atmosphere code, to obtain spectra that could be compared to observations.

Bibliography

Banerjee, R. and R. E. Pudritz, 2007: Massive star formation via high accretion rates and early disk- driven outflows. *Astrophysical Journal*, **660**, 479–488, doi: http://dx.doi.org/10.1086/512010.

Baraffe, I., G. Chabrier, and T. Barman, 2010: The physical properties of extra-solar planets. *Reports on Progress in Physics*, **73 (1)**, 016 901, URL `http://stacks.iop.org/0034-4885/73/i=1/a=016901`.

Burrows, A., W. B. Hubbard, J. I. Lunine, and J. Liebert, 2001: The theory of brown dwarfs and extrasolar giant planets. *Reviews of Modern Physics*, **73 (3)**, 719–765.

Chabrier, G., F. Allard, I. Baraffe, T. Barman, and P. Hauschildt, 2004: The physics of extrasolar gaseous planets : from theory to observable signatures. *ASP Conference Series*.

Chandrasekhar, S., 1957: *An introduction to the study of stellar structure*. Dover publications, inc., 509 pp.

Colella, P. and H. M. Glaz, 1985: Efficient Solution Algorithms for the Riemann Problem for Real Gases. *Journal of Computational Physics*, **59**, 264–289.

Colella, P. and P. R. Woodward, 1984: The Piecewise Parabolic Method (PPM) for Gas-Dynamical Simulations. *Journal of Computational Physics*, **54**, 174–201.

Couch, S. M., D. Pooley, J. C. Wheeler, and M. s. Milosavljevic, 2011: Aspherical supernova shock breakout and the observations of supernova 2008d. *The Astrophysical Journal*, **727 (2)**, 104, doi:http://dx.doi.org/10.1088/0004-637X/727/2/104.

de Val-Borro, M., P. Artymowicz, G. D'Angelo, and A. Peplinski, 2007: Vortex generation in protoplanetary disks with an embedded giant planet. *Astronomy and Astrophysics*, **471**, 1043–1055, doi:http://dx.doi.org/10.1051/0004-6361:20077169.

Dorfi, E. A., 1998: Radiation Hydrodynamics: Numerical Aspects and Applications. *Computational Methods for Astrophysical Fluid Flow*, Spriger-Verlag.

Freytag, B., F. Allard, H. G. Ludwig, D. Homeier, and M. Steffen, 2010: The role of convection, overshoot, and gravity waves for the transport of dust in M dwarf and brown dwarf atmospheres. *Astronomy and Astrophysics*, **513**, A19.

Fryxell, B., et al., 2000: Flash: An adaptative mesh hydrodynamics code for modeling astrophysical thermonuclear flashes. *The Astrophysical Journal Supplement Series*, **131**, 273–274.

Godunov, S., 1959: A Difference Scheme for Numerical Solution of Discontinuous Solution of Hydrodynamic Equations. *Math. Sbornik*, **47**, 271–306.

Hansen, C. J. and S. D. Kawaler, 1994: *Stellar interiors. Physical priciples, structure and evolution*. Springer-Verlag, 445 pp.

Hauschildt, P. H. and E. Baron, 2011: A 3D radiative transfer framework VIII. OpenCL implementation. *Astronomy and Astrophysics*, **533**.

Kippenhahn, R. and A. Weigert, 1991: *Stellar structure and evolution*. Springer-Verlag, 468 pp.

Ludwig, H.-G., 2006: Prospects of using simulations to study the photospheres of brown dwarfs. *Convection in Astrophysics. Proceedings IAU Symposium No. 239*, International Astronomical Union. F. Kupka, I. W. Roxburgh & K. L. Chan, eds., 205–210.

MacNeice, P., K. M. Olson, C. Mobarry, R. deFainchtein, and C. Packer, 2000: PARAMESH : A parallel adaptive mesh refinement community toolkit. *Computer Physics Communications*, **126**, 330–354.

Mihalas, D. and B. W. Mihalas, 1984: *Foundations of radiation hydrodynamics*. Oxford University Press, 717 pp.

Smith, W. R. and R. W. Missen, 1982: *Chemical reaction equilibrium analysis: theory and algorithms*. John Wiley and Sons, 190 pp.

Stein, R. F. and A. Nordlund, 1998: Simulations of Solar Granulation. I. General Properties. *The Astrophysical Journal*, **499**, 914–933.

Strang, G., 1968: On the construction and comparison of different splitting schemes. *SIAM Journal on Numerical Analysis*, **5 No.3**, 506–517.

Toro, E. F., 2009: *Riemann solvers and numerical methods for fluid dynamic*. Springer-Verlag, 724 pp.

Wende, S., A. Reiners, and H.-G. Ludwig, 2009: 3D simulations of M star atmosphere velocities and their influence on molecular FeH lines. *Astronomy and Astrophysics*, **508**, 1429–1442.

Whitworth, A. P. and D. Stamatellos, 2006: The minimum mass for star formation, and the origin of binary brown dwarfs. *Astronomy and Astrophysics*, **458**, 817–829.

Witte, S., C. Helling, and P. H. Hauschildt, 2011: Dust in brown dwarfs and extra-solar planets III. Testing synthetic spectra on observations. *Astronomy and Astrophysics*, **529**.

Acknowledgement

Many people contributed in one way or another to this work. I wish to thank my advisor Peter Hauschildt for his support and encouragement whenever I needed it. I would also like to thank:

- Sebastian Knop, who was a great guide, supportive officemate, was my FLASH interlocutor, introduced me to vi and taught me German with “5 mal 5” and Loriot sketches.
- Soeren Witte, who not only provided the PHOENIX/1D models that allowed me to set and test my simulations, but was also a helpful proofreader, patient officemate and chocolate provider.
- Dennis Jack and Eddie Baron for the very fruitful discussions on the internal energy that were crucial in the last stages of my PhD.
- Mariana Wagner who was the perfect travel companion: I am glad the proximity of our subjects allowed us to go to a couple of conferences together.
- Andreas Schweitzer for the technical support, scientific advice and for for proofereading parts of my thesis.
- Andreas, Alex, Marlies, Ernst, Carolina, Anna-Lea and the rest of group members and observatory colleagues for their support and enjoyable company.
- Lalitha, for offering me her sofa, preparing me the most delicious dinners and distracting me on the night before the ”dispu”.
- The observatory staff who made my life in Hamburg so much easier.
- The HmbNFG and the GRK 1351 for the financial support.

I want of course to thank my family and friends, for backing everyone of my wishes and ideas. Finally I want to thank Daniel, who always managed to make me laugh and move forward.